EFFECTS OF HIGHLY POROUS COMPONENTS ON HYDRAULIC CONDUCTIVITY OF SIMULATED GRANULAR MIXTURES

A Thesis
Presented to
The Academic Faculty

by

Sean Matthew Tyndale

In Partial Fulfillment
of the Requirements for the Degree
Master of Science in the
School of Civil and Environmental Engineering

Georgia Institute of Technology
May 2021

COPYRIGHT © 2021 BY SEAN MATTHEW TYNDALE

EFFECTS OF HIGHLY POROUS COMPONENTS ON HYDRAULIC CONDUCTIVITY OF SIMULATED GRANULAR MIXTURES

Approved by:

Dr. Susan Burns, Advisor
School of Civil and Environmental Engineering
Georgia Institute of Technology

Dr. Sheng Dai,
School of Civil and Environmental Engineering
Georgia Institute of Technology

Dr. J. David Frost
School of Civil and Environmental Engineering
Georgia Institute of Technology

Date Approved: January 22, 2021

To my Mom, Charlotte Charbit, and all my supportive friends and family

ACKNOWLEDGEMENTS

The acknowledgements of this report go to my advisor Dr. Susan Burns. Her continuous support, encouragement, enthusiasm, patience, kindness, and belief in me has been unwavering since my first class of hers at Georgia Tech as a transfer student to my last days as her research assistant here at Georgia Tech. I am especially thankful for her providing me with the freedom, resources, and guidance to explore this research. Her respect and love for research is a true inspiration, and has guided me to grow and to push my own abilities in research that I never thought possible. I will always be grateful to her. I would secondly like to thank my Mom (Marchia Hammond), Grandpa (Basil Roberts), and Uncle (Neil Roberts) for being there for me and pushing me to pursue my education and dreams as far as they can go. My mom has always been my hero, and has always taught me that the only limits we have are the ones that we set upon ourselves. I would also like to thank my loving best friend Charlotte Charbit for always being there for me with her endless support and kindness. I would like to thank Dr. Chloe Arson and Dr. Susan Burns for allowing me the great opportunity to study my research with Dr. Laurent Brochard at Ecole des ponts Paris Tech. I would like to thank Dr. Xenia Wirth who helped lead me through the foundations in my experimental plan, and has had constant presence and guidance throughout my research. Her along with the rest of my group (Hejintao, Lynnae, Junghwoon, Youngsuk, and Shaivan) have all been a great inspiration as well as great friends to me, and I am so thankful to all of them for the great company and conversations in the past few years. The same goes to all my friends in the geosystems department. I would like to acknowledge Andy Udell and all of his hardworking team in the machine shop for their help in my experimental setup and obstacles. I would like to thank the faculty

of the geosystems department for being such thoughtful academic professors, and that includes my committee members. They have all had a hand in the development of my research from Dr. Frost aiding me to retrofit some of the triaxial equipment, offering excellent advice on reading papers effectively, and always providing a larger perspective to engineering. Thanks goes to Dr. Burns again as she gave me my first experimental research opportunity to work with Dr. Sheng Dai as an undergraduate, and he gave me a chance to become involved in experimental research. Those were the days I thought back to the most during this later portion of my research. Now I feel that I have just started to develop an intimate experimental relationship, and I constantly thought back to learning under Dr. Jongchan Kim, and how he would always ask the question “why” when he too faced obstacles. He would come up with a plan and move forward. The drive to keep understanding and pushing the envelope of the unknown regardless of countless failures that may lie ahead. I feel this is what research has taught me the most, and it has made me learn to understand a lot about myself, and what I want to do with the skills I have obtained from my time at Georgia Tech. I am so thankful to have these memories, experiences, and friends to look back on in my life.

TABLE OF CONTENTS

LIST OF TABLES

LIST OF FIGURES

SUMMARY

Fly ash is the lightweight byproduct that results from the combustion of coal during production of various commodities and services including electricity. In the United States, millions of tons of fly ash are generated each year in producing electricity. Approximately 40.0% of this combustion byproduct is beneficially used in applications including concrete, fills, and construction materials; however, the remaining 60.0% is geologically disposed. Historically, this ash is disposed of into surface ponds open to weathering and long-term geochemical alteration. Most significantly, this weathering can contribute to changes in the particle mineralogy, surface charge, and surface area, which in turn impact the hydraulic conductivity of the fly ash deposit. While the hydraulic conductivity of fly ash is typically similar to that of silt-sized soils, it is not uncommon to encounter pockets of fly ash that are not easily dewaterable; that is, some fly ash deposits exhibit significant water retention capacities. The work performed in this study investigated the hydraulic properties of a model particulate mixture that was composed of fine sand particles and highly porous additives including diatomaceous earth (DE) and activated carbon (AC). The highly porous additives were chosen as representative of natural materials that are commonly observed in ponded fly ash (i.e., diatoms and partially combusted carbon). Fine sand (sieved F110) was chosen as the representative matrix particulate media, and DE and AC were mixed with the sand at percentages of 2.5, 5.0, and 10.0%. The highly porous mixtures were different in nature because the DE particles were small enough to occupy the void spaces of the sand, while the AC particles were large compared to the sand grains, and existed as discrete particles in the mixture, not only occupying pore spaces between sand grains.

Limiting void ratio tests demonstrated that the presence of the DE and the AC had significant impact on the fabric and structure of the mixtures, as the % high porosity components in the mixture were increased from 2.5% to 5.0% to 10.0% by volume. For mixtures with high porosity additives, e_{max} increased in all cases (from 0.84 with 100% sand to 1.37 for the sample with 10.0% DE / 90.0% sand and to 0.98 for the sample with 10.0% AC / 90.0% sand). These data show that a higher void ratio was achieved with the inclusion of these components, which is attributable to the high porosity in these additional particles and to the less efficient packing of angular particles when mixed with sand. These same impacts on packing were observed in e_{min}, with the minimum void ratio increasing from 0.55 for 100% sand samples to 0.59 for 10.0% DE and 0.68 for 10.0% AC samples, indicating less efficient packing for the samples when sand was replaced with the high porosity components.

Measured values of hydraulic conductivity indicated that the highly porous components decreased the saturated hydraulic conductivity by one to two orders of magnitude. The DE particles were small enough to fill the void spaces of the sand matrix, while the AC particles had a larger range in grain sizes, and both packed void space, or displaced sand grains. Addition of these highly porous components act to reduce the hydraulic conductivity, and will also act to retain water in partially saturated conditions due to high capillary forces within their highly porous structure.

CHAPTER 1 INTRODUCTION

1.1 MOTIVATION

Production of energy is central to creating a higher standard of living for human beings, for creating and maintaining infrastructure, and for operating all aspects of the transportation sector; consequently, energy recovery, production, and disposal impact nearly all sectors of contemporary society. Domestic energy use in the United States exceeded the amount of energy produced by the United States in 2019, requiring import of energy from overseas [1]. The US is also the global leader in fossil fuel as their consumption per capita is more than that of any other nation in the world as of 2019 [2]. While petroleum is the primary fossil fuel that provides energy for transportation systems, electricity is primarily generated from fossil fuels including coal and natural gas, as well as some oil [3]. Traditionally, coal was one of the most dominant sources of energy in the United States, with 539 million tons of coal combusted annually (2019), roughly 11.0% of the total energy consumption in the United States [4]. However, improved technologies to recover natural gas have had a significant impact on the generation of energy for the power industry, resulting in a decreased level of coal combustion by approximately 20.0% in the past 15 years [5]. Globally, coal combustion accounts for roughly 38.0% of the energy produced [5], with roughly 30.0% of electricity in the United States being generated from coal combustion [5].

Over recent decades, society has developed a more environmentally conscious mindset for long term planning and design to utilize resources sustainably to maximize the benefit of those resources, with increased levels of recycling or beneficial use in

appropriate applications. Simply increasing the life span of constructed infrastructure or using waste materials beneficially will reduce the use of virgin materials in construction, as well as the quantity of waste for disposal. Recent attention has focused on more efficient utilization of resources, especially when resources are limited in supply or there are environmental concerns upon release to the environment, impacting local ecosystems as well as global ecosystems (e.g., CO_2 emissions). Current initiatives and projects focused on the recycling of waste byproducts include such applications as technologies to capture CO_2 emissions and eventually store them for further use [6]; however, there remain technical difficulties and many obstacles in order for civil and environmental engineers to understand how best to store, capture, and handle waste materials so they can be beneficially used.

All methods of combustion of fossil fuels produce a carbon footprint and waste products. In addition to CO_2, combustion of coal produces solid residuals because approximately 40.0% of the coal solid is not combustible, and does not convert into energy. Solid residuals from the combustion of coal are known as coal combustion products (CCPs) and include fly ash, bottom ash, boiler slag, and flue gas desulfurization gypsum. While each of these residuals have applications for beneficial use, the work in this thesis will focus on fly ash, the low density CCP that is collected at the discharge from the combustion chamber. Fly ash is defined as "the finely divided residue that results from the combustion of pulverized coal and is transported from the combustion chamber by exhaust gases" [7]. This finely divided residue is roughly a silt-sized material, with hollow spherical particles composed of aluminosilicate and amorphous materials.

Fly ash is produced in combustion-based power plants that generate steam to produce electricity by utilizing coal as the power source [7]. The coal is usually pulverized and then placed and ignited in a boiler combustion chamber where it becomes molten mineral, generating heat that is extracted from a tube system in the boiler [7]. That molten mineral and flue gas eventually cool down, forming a solid ash [7]. This solid ash is categorized into various types of ash: coarse, dense particles that fall to the bottom of the combustion chamber, known as bottom ash or slag [7], and lighter ash particles that remain suspended in the cooling flue gas, and are removed with particulate emission control devices called filter fabric baghouses or electrostatic precipitators [7]. In 2010, approximately 43.0% of fly ash produced in the US was beneficially used in civil engineering applications, such as concrete or fills [8]. An ACAA survey reported that the 43.0% of beneficial use applications were distributed as follows: 32.0% used in construction and civil applications, 9.9% in mining applications, and 1.1% for other various applications [8]. With improved technologies and global initiatives for sustainable development, the applications of CCP will continue to grow with new possible applications developing for the remaining 57.0% that is not currently beneficially used [8]; currently, those materials are being disposed into landfills, ash ponds, and dry silos.

In terms of the civil engineering applications of fly ash, approximately 20 million metric tons of fly ash are utilized as supplementary cementitious materials, road stabilizers, grouts, asphalt fillers, structural fill, soil stabilization, and many other applications [9]. Fly ash has some unique properties that make it suitable for these applications, both in terms of its physical and chemical makeup, allowing it to be incorporated into concrete, while benefiting the overall utility of these applications. This creates major incentives to utilize

the coal combustion products, and has significant environmental impacts according to the U.S. Department of Transportation's Federal Highway Administration, which suggests that the utilization of fly ash in concrete applications can benefit the environment by increasing project life of roads and infrastructure by improving the durability of the concrete. It also reduces net energy and greenhouse gasses when fly ash is used as a replacement for cement [9]. However, as Ramme and Tharaniyil (2013) note the total repurposing of this material only amounts to approximately 43.0% annually across several industries [8]. The remaining 57.0% of the material is being stockpiled or being disposed of into landfills on an annual basis [8]. The roughly 43.0% of CCPs that are beneficially used are typically sold directly from the production plant, dry processed into storage, or conditioned for future use (Figure 1). Of the 57.0% CCPs that are not beneficially used, disposal applications traditionally include landfilling, or sluicing to an ash pond, followed by gravity settling and land disposal [9].

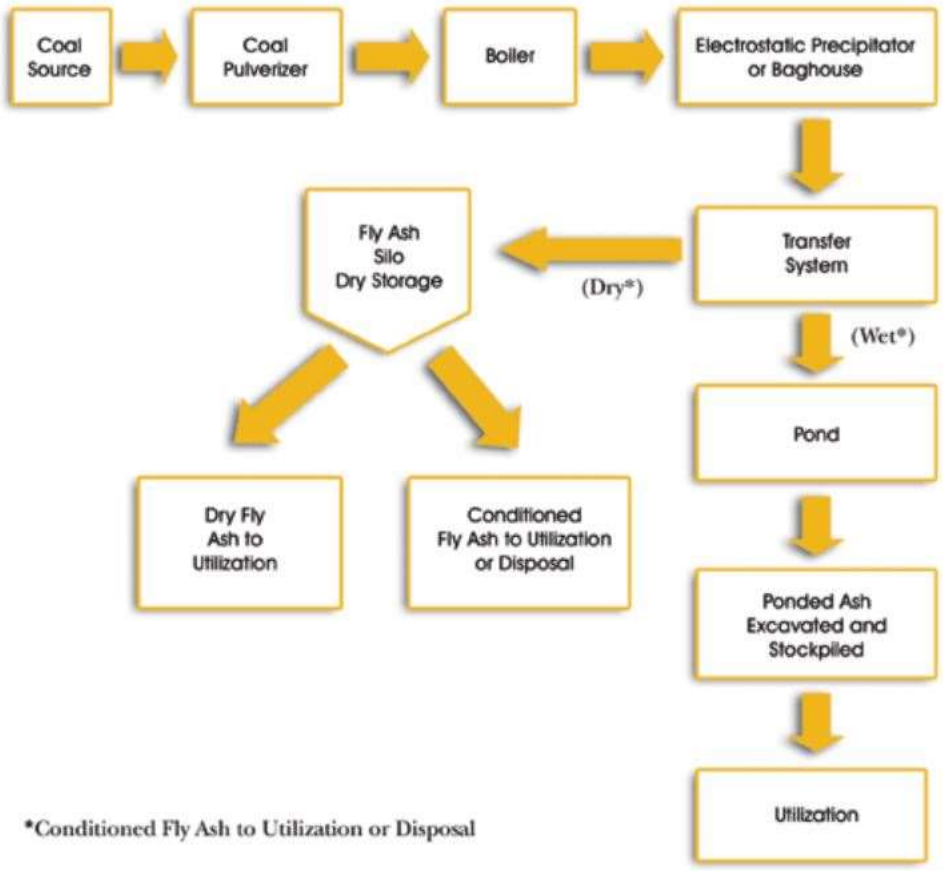

Figure 1: Life cycle flow chart of fly ash. (Figure from U.S. Department of Transportation Federal Highway Administration [9]).

It is important to note that land storage of fly ash allows future harvesting for beneficial use options. Fly ash sources for later utilization are usually placed into dry landfills or silos, where they are stored, maintained, and eventually utilized in later times of limited supply, for example, during periods of moderate temperatures, with limited coal combustion for electricity generation. With growing beneficial use opportunities for fly ash in emerging innovative applications, along with the steady decline of the overall energy generation using coal-based power in the United States, demand for stored CCPs is anticipated to increase [10]. Consequently, dry storage of ash is the preferred alternative

for three reasons: it is less energy intensive to recover the ash for beneficial use, the geotechnical stability of the deposit is higher, and the environmental impact due to contaminant leaching is lower.

Historically, the sluiced disposal of fly ash through ponding resulted in long term management issues in terms of geotechnical stability. For example, the Tennessee Valley Authority's (TVA) Kingston Fossil Plant located in Roane, Tennessee included a disposal facility, designed to store fly ash and ultimately settle the deposits in a 34-hectare (84-acre) dewatering pond [11]. In 2008, one of the dikes that was used to contain the ash ruptured, releasing approximately 1.3 x 10^6 m^3 (4.6 x 10^7 ft^3) of fly ash into the surrounding communities and nearby water streams and ecosystems (Figure 2), covering an area of approximately 120 hectares (300 acres) (Figure 3) [11].

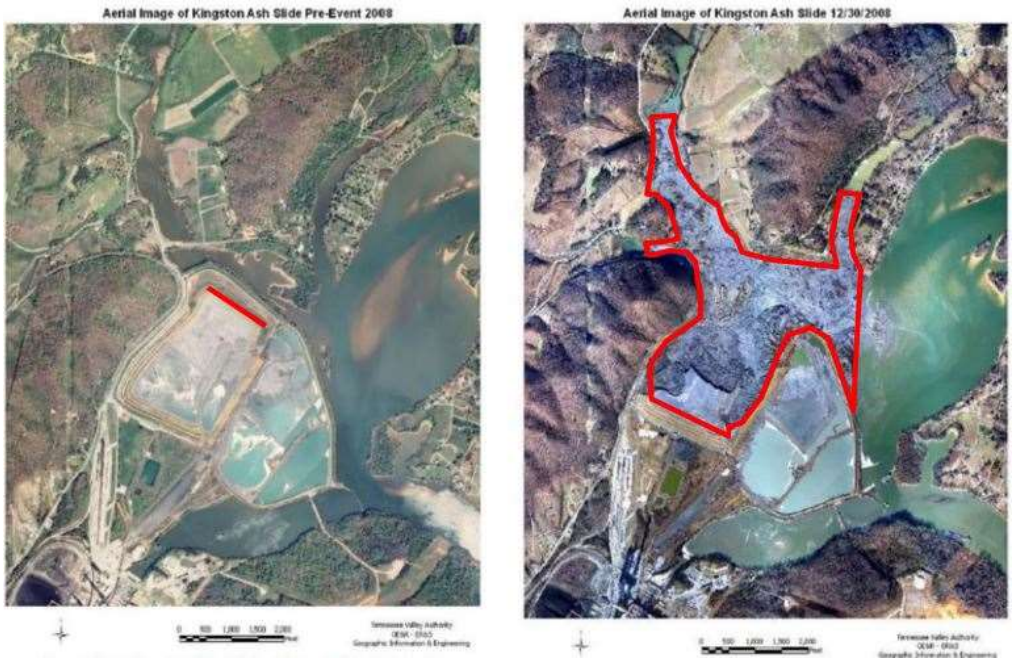

Figure 2: Side by side image of TVA Kingston Fossil Plant before and after spill. Red line delineates location of ruptured dike. Red polygon delineates spread of spilled fly ash into environment. (Figure from Tennessee Meteorite Site at Center of TVA Coal Compliance Issue [12].)

Figure 3: Damaged property from TVA Kingston fly ash spill. (Figure from *The New York Times Company* [13]).

Following the 2008 rupture of the dikes at the Kingston Plant, the Environmental Protection Agency (EPA) changed the regulatory framework for disposal of fly ash, requiring closure that met enhanced stability and environmental standards [14]. Seven years after the TVA pond failure in 2015, the EPA established a final rule for handling and disposal of fly ash [14]. Under these regulations, ash ponds are subjected to frequent monitoring, and disposal of new CCPs is required to be in a permitted landfill. Under the five-year closure rule established in by the EPA, legacy deposits in ash ponds that do not meet current stability standards are required to remediate the deposit and often export the material to permitted landfill facilities that were designed and constructed to current standards. The excavation and transport is complicated by the fact that the fly ash in the ponds is often in a saturated condition, requiring drainage to a moisture content that makes handling and transportation less energy intensive. Consequently, ongoing management of ash ponds requires careful maintenance and dewatering of these legacy deposits. In some cases, it has been observed that ash drains reasonably easily, while other ash deposits, with similar characteristics, are difficult to drain, and retain high moisture contents, even under long term, drained conditions.

Because a significant percentage of fly ash cannot currently be beneficially used, geologic disposal will continue to be a necessity. Consequently, handling and maintenance of ash deposits will continue to prove challenging, especially in cases where the ash is not free draining. The work performed in this thesis focused specifically on the characterization of high surface area / high porosity components in particulate media and their impact on the hydraulic conductivity of a fine sand. Diatomaceous earth (DE) and activated carbon (AC) were chosen as the high porosity component simulants because diatoms and their

residuals are commonly found in fly ash deposits, and activated carbon is very similar to the unburned carbon phase that is present in off-specification fly ash. Off specification ash cannot be used in concrete due to high loss-on-ignition values, which are excluded in the ASTM standard for fly ash applications in concrete. While fly ash is a silt-sized material, fine sand was chosen as the representative particulate media for testing, as opposed to a silt, due to ease of specimen preparation and experimentation. Sand mixtures were created with highly porous components up to 10.0% by volume and the saturated hydraulic conductivity was measured as a function of relative density and mixture percentages.

CHAPTER 2 CHARACTERIZATION AND ENGINEERING BEHAVIOR OF FLY ASH

Fly ash is a silt-sized particulate media, composed of hollow aluminosilicate spheres and amorphous phases that form during the combustion of coal. After coal is combusted, the residual products are collected for beneficial use or disposal. Historically, fly ash is collected from electrostatic precipitators, mixed with water, and sluiced to an ash pond, where it is allowed to gravity settle. More recent regulations require fly ash to be landfilled in dry form in a lined, Subtitle D landfill. For ash that can be beneficially used, the ash is typically sold directly from the point of production or from dry storage stacks.

While ponding of ash has historically been considered a medium to long-term disposal solution, ongoing maintenance activities at a plant may require access to ash stored in the ponds. Additionally, movement of the ash can be necessary for a multitude of reasons, such as slope stabilization or transportation to a newly constructed regulated facility, so it is not uncommon to relocate ash located from storage on-site at a power plant. Ponded ash is often saturated within the deepest portions of the storage pond, but partially saturated near the pond surface; that is “ponded” does not necessarily imply saturation of ash that has been disposed. Maintenance of ash stored in the wet condition frequently requires access using excavating equipment, often to facilitate drainage.

For applications in concrete, fly ash is categorized according to source coal (e.g., anthracite, bituminous, sub-bituminous) and material properties. Class F fly ash results

from the combustion of anthracite or bituminous coal and has pozzolanic properties to react with calcium hydroxide and form cementitious phases [15]. Class C fly ash results from the combustion of lignite or subbituminous coal, and is self-cementing in addition to exhibiting pozzolanic properties [15]. Both types of ash are useful in concrete applications due to the pozzolanic reaction that allows greater ultimate strength to be achieved in concrete when compared to cement only concrete [15]. The addition of fly ash to concrete is also beneficial due to increased workability of the resulting concrete.

2.1 Drainage of Ponded Fly Ash

Ultimately, free drainage of any particulate material is critical to ensure geotechnical stability. Sources of water retention in fly ash can include mechanisms that occur during placement and installation (e.g., layered fine/coarse grained structures), during long term storage (e.g., dissolution/precipitation of hydrated mineral phases), or during drainage periods (e.g., clogging due to particle migration). Consequently, understanding of the underlying mechanisms that are controlling drainage patterns is important.

Pore fluid saturated conductivity in fine-grained soils can be described using the Kozeny-Carman equation, which quantifies and predicts permeability of a particulate media [16]. This equation is often used to describe fluid flow through a range of particles sizes, and can be applied to non-plastic silts under laminar flow conditions [16] and [17]:

$$k = \left(\frac{\gamma}{\mu}\right) * \left(\frac{1}{C_{K-C}}\right) * \left(\frac{1}{S_0^2}\right) * \left[\frac{e^3}{1+e}\right] \quad (1)$$

Where γ is the unit weight of the permeant; C_{K-C} is Kozeny-Carman's empirical coefficient (usually taken to be equivalent to 5); μ is the viscosity of the interacting fluid; e represents void ratio of particle system; S_0 represents specific surface area for every unit volume of particles within the system [16].

Because water flows through the pore spaces in a particulate media, decreasing cross-sectional area of these pore spaces will result in an increase in velocity, assuming the flowrate is constant. Additionally, as the pressure gradient across the particulate media decreases, the flowrate through the porous media would also decrease. While class C fly ash is defined as having self-cementing properties, the degree of self-cementation is a function of the specific ash properties and can vary between samples [18]. Cementation causes clogging, which will impact the hydraulic conductivity of the fly ash, where highly self-cementing ash can have a conductivity that is three orders of magnitude lower than ashes that exhibit lower self-cementation [18]. As cementation develops, the shape of the pore space will change over time, and when compared to the shape of the pore space in uncemented porous media, cemented fly ash can form uneven internal porous structures or capillary tubes that hinder drainage, forming bottle neck pores, for example (Figure 4).

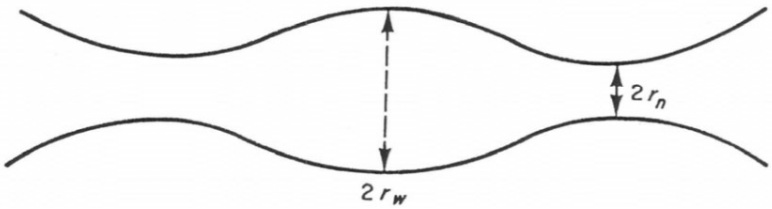

Figure 4: Diagram of irregular internal porous structures that are prone to capillary condensation (figure from Departments of Chemical Engineering and Chemistry, Brigham Young University) [19].

During drainage of fly ash, gas and/or vapor can collect in the pores, forming an internal meniscus within the pore space, which facilitates retention of pore fluid in a fine-grained particulate media like fly ash. This is especially common in soils with micro to nano-sized pores that have dissolved salts in the pore fluid, where van der Waals forces can be relatively high [20]. Ultimately, this can lead to interaction of water vapor with the inner walls of the capillaries, a process known as capillary condensation [19], where the bottle neck pore spaces can retain fluid within the pore space, requiring application of energy to drain the pores. This scenario is most likely to occur in ponded fly ash during drainage or during changing seasons and temperature swings, as it is a listed requirement for facilities to periodically monitor the CCP levels in relation to the water surface. This facilitates assessment of potentially hazardous high water pressure conditions; thus, creating the development of partially saturated zones in ash ponds [21].

In addition to the aluminosilicate fly ash cenospheres, ponded fly ash typically contains mineral and amorphous phases, such as unburned or partially combusted organic matter, hydrated mineral phases, silica particles carried over from boiler operations, or residual local soil mixed in during disposal operations [22]. As such, it is useful to examine the development of capillary pressure within the fly ash as a function of grain or pore size. For the purposes of this review, a model was developed in collaboration with Dr. Brochard from Ecole des Ponts to quantify capillary pressure in fly ashes with varying pore sizes. Mixture behavior is well documented in soil behavior, impacting strength, stiffness, and conductivity in a variety of applications. The model described here is based on the assumptions that: (1) fly ash is a mixture that can be described with nonreactive spherical particles (fly ash) mixed with porous or nonporous grains that are combined with the

spherical ash particles (e.g., activated carbon, or diatomaceous earth); (2) that the Kozeny Carman equation applies to the unsaturated mixture; (3) that there is laminar flow drainage; (4) that osmotic equilibrium is reached; and (5) that chemical potential and temperature are uniform across the mixture [16].

The previous assumptions allow three regimes to be modeled as the equilibrium of gravitational forces (drainage) and capillary forces (retention) acting on the water phase between the particles, resulting in partial saturation when force equilibrium is reached (Figure 5). The capillary forces are a function of pore size and can be greater than, equal to, or less than the gravitational forces in a porous media (Table 1). The rate of flow within the system of particles is denoted as $\frac{dh}{dt}$ and is a function of the hydraulic conductivity of the soil, the pressure head difference, and the fluid properties. Note that capillary forces are denoted as P_{cap} with gravitational forces denoted as P_{grav}, where P represents the forces over the area of the particles, where they create opposing pressure on the system.

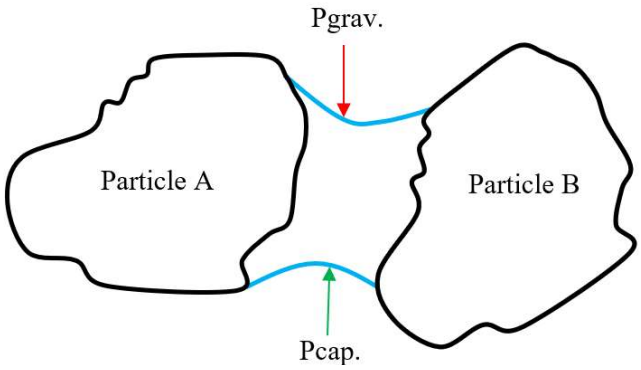

Figure 5: Force equilibrium reached with water meniscus between particles.

Table 1: Conditions of Force Equilibrium for Drainage Regimes

Force Balance	$\boldsymbol{\frac{dh}{dt}} =$	**Qualitative Explanation**
$P_{cap} \gg P_{grav}$ (Using imbibition)	$-\frac{k}{\mu}\frac{2\gamma}{rh} \rightarrow \frac{h_f^2 - h_0^2}{2} = \frac{k}{\mu}\frac{2\gamma}{rh} * t$	Capillary forces dominate the gravitational forces; fly ash does not desaturate due to imbibition between the particles
$P_{cap} \gg P_{grav}$	$-\frac{k}{\mu}\frac{2\gamma}{rh} \rightarrow \frac{h_f^2 - h_0^2}{2} = \frac{k}{\mu}\frac{2\gamma}{rh} * t$	Capillary forces dominate the gravitational forces; fly ash does not desaturate
$P_{cap} \ll P_{grav}$	$-\frac{k}{\mu} * \rho g \rightarrow h_f^2 - h_0^2 = \frac{k}{\mu} * \rho g * t$	Gravitational forces dominate the capillary forces during drainage until equilibrium is achieved with capillary forces. Partial saturation
$P_{cap} = P_{grav}$	0	Intermediary situation where forces compensate, and flow stops at the height of capillary rise when $\frac{dh}{dt} = 0$

These equations can be simplified as described in the following:

$$P_{cap} \approx \frac{2\gamma}{\mathrm{r}} \quad \text{and} \quad P_{grav} \approx \rho g L \tag{2}$$

Where r = radius capillary (mean pore size – found from pore size distribution); $\gamma =$ surface tension ($\gamma = 0.07 \frac{N}{m}$); $\rho = \frac{10^3 kg}{m^3}$ = density of water; and $g = 9.81 \frac{m}{s^2}$ = acceleration due to gravity.

Assuming representative values for a specimen of fly ash in a partially saturated laboratory experiment (r =.000015 m and L = 0.127 m), demonstrates that the capillary force in a typical fly ash material is larger than the gravitational forces by almost an order of magnitude:

$$P_{cap} \approx \frac{2\gamma}{r} = \frac{2*0.07\frac{N}{m}}{0.000015 \text{ m}} = 9{,}333\ N >> P_{grav} \approx \rho g L = \frac{10^3 kg * 9.81 m}{m^3 * s^2} * 0.127 m = 1245\ N$$

2.2 Capillary Pressure and Fly Ash Grain Size

The capillary pressure is directly influenced by including highly porous materials in soil mixtures due to changes in the mean pore size. For example, mixing particles like activated carbon (highly porous with small void spaces) into a blend with fly ash reduces average pore size, making the capillary force greater, which results in increased retention of water within the mixture. While methods exist to measure pore size (e.g., mercury intrusion porosimetry), it is more practical to measure grain size and total surface area as analogues for pore size. Wirth (2019) performed particle size analysis of ponded fly ash from a power plant in the southeastern United States using ash samples obtained from two boreholes (BH-2 and BH-10) (Figure 6).

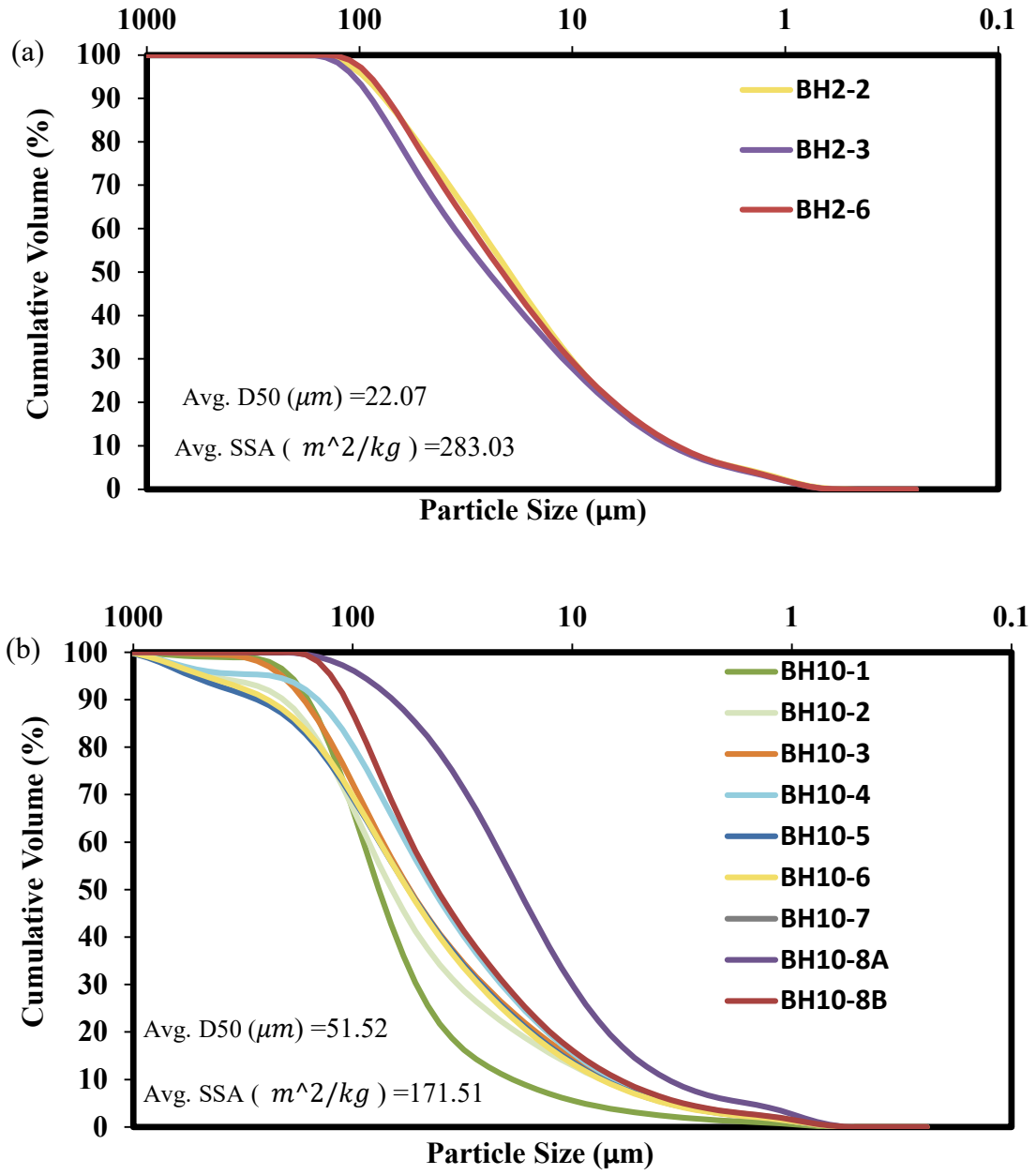

Figure 6: Particle size analysis for ponded fly ash in the southeastern United States: (a) BH2 sample analysis and (b) BH10 [22] (Figures from Wirth (2019)).

Wirth's (2019) data confirm that fly ash is a silt-sized material, with specific surface area values for fly ash on the order of 85 to 300 m^2/kg (Table 3). These data are in agreement with other tests of pure fly ash samples (e.g., Kim 2005) (Figure 7). Yeboah (2013) measured grain size distributions for thirteen pure coal ash samples that were collected in total from 8 different plants [23]. The first five plants provided 3 samples (1 pure coal fly ash and 2 biomass ashes from co-firing tests) [23]. The last 3 samples (BP1, BP2, and BP3) were biomass fly ash from "mill waste, logging, or urban woodwaste without any coal", which demonstrated significantly larger particle sizes than the coal fly ash, but also significantly larger specific surface areas, indicating the presence of a large number of small pores within the biomass ash [23] (Figure 8). The grading of the grain size distribution is an important consideration as well because the grade can categorize material based on particle size to give insight for other characterization properties, particularly the hydraulic properties. Grain size distributions of fly ash tend to be uniformly graded (Figure 8).

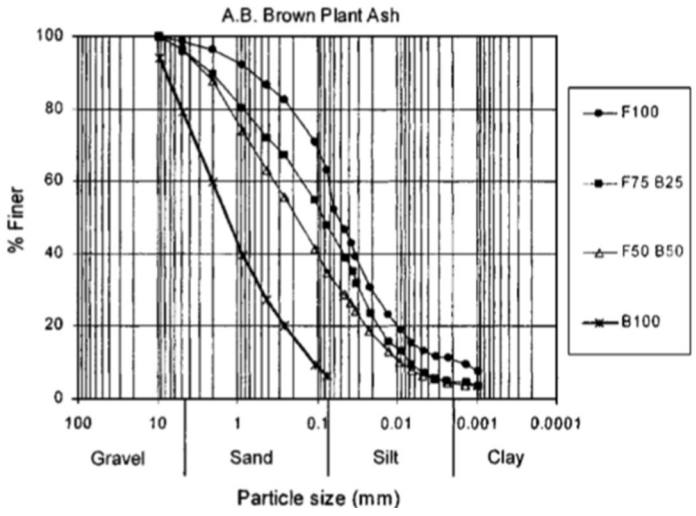

Figure 7: Grain size distribution of pure fly ash (F100) (Figure from [24]).

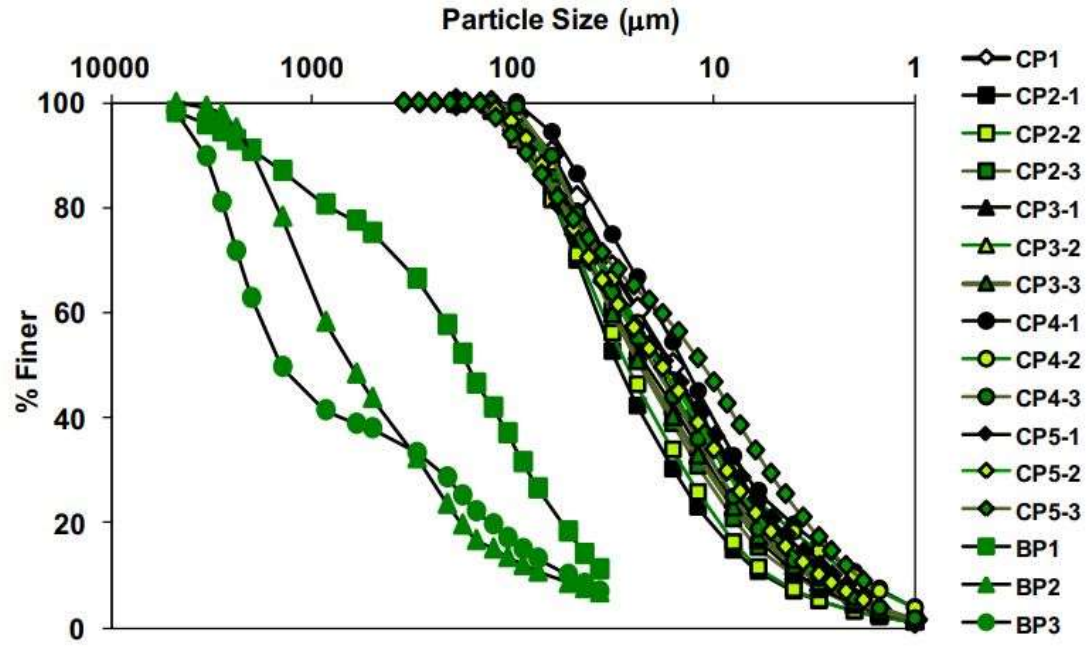

Figure 8: Grain size distribution of biomass fly ash and coal fly ash (figure from [23]).

2.3 Saturated Hydraulic Conductivity of Fly Ash

In terms of engineering behavior, studies that have quantified the hydraulic conductivity of pure fly ash are relatively limited; however, most report values are on the order of 1x 10^{-5} to 1 x 10^{-6} cm/sec, which is consistent with the particle grain size. For Class F fly ash, Mollamahmutoglu (2001) reported value of hydraulic conductivity k = $4.4x10^{-05}\,\frac{cm}{s}$ [25]; Kim (2005) reported two similar values for samples of fly ash: Wabash River Plant with hydraulic conductivity $k = 3x10^{-06}\,\frac{cm}{s}$ and the A. B. Brown Plant ash with $k = 6x10^{-06}\,\frac{cm}{s}$ [24]; and Ghosh (2020) reported a value k = $4.5x10^{-05}\,\frac{cm}{s}$ (Table 2).

Table 2. Hydraulic Conductivity Values for Class F Fly Ash

Hydraulic Conductivity (cm/s)	Class	Reference
4.4×10^{-5}	F	(M. Mollamahmutoglu, 2001)
3×10^{-6} and 6×10^{-6}	F	(Bumjoo Kim, 2005)
4.5×10^{-5}	F	(A. Ghosh, 2020)

2.4 Fly Ash Characterization

In addition to grain size distribution, fly ash characterization data generally include residual unburned carbon content, which is commonly quantified using the Loss on Ignition (LOI) test, plasticity (primarily liquid limit (LL)), and specific surface area (SSA). A review of the literature demonstrated LOI values normally less than 6.0% for beneficial use ash, although some are substantially higher (Table 3). A value of LOI below 6.0% is important for beneficial use of fly ash in concrete because high LOI values often interfere with the chemical admixtures in concrete. Measured values of LL for fly ash are typically less than 50.0% [26], with treatment or ponding reducing that value even further [22].

Table 3. Characterization Properties of Fly Ash*

Class	LOI (% Comp.)	LL (%)	D50 (μm)	SSA ($\frac{m^2}{kg}$)	Reference
F	-	-	-	280.0	(A. Mneina, 2017)
F	-	-	-	328.9	(Surender Singh, 2018)
-	3.59	-	-	360.0	(Ana M. Fernandez Jimenez, 2006)
-	2.12	-	-	-	(Gengying Li, 2005)
-	18.18	-	19.5	-	(Bidula Bose, 2012)
C	1.19, 1.10	-	-	-	(Erdal Çokça, 2001)
F	3.1	43.0%	-	426.0	(Arvind Kumar, 2007)
	2.1	-	-	565.0	(Gengying Li, 2003)
F	2.88	-	-	-	(Graciela M. Giaccio, 1988)
F	-	-	-	-	(Ping-Chung Kao, 2000)
-	28.5 (dry wt.)	-	-	-	(A. Polettini, 2004)
-	3.9	-	-	396.0	(Shi Cong Kou, 2007)
-	-	-	-	-	(S. M. Pathan, 2003)
F	-	-	30	-	(M. Mollamahmutoglu, 2001)
-	7.2 2.6 1.4	44.0 to 62.0%	10.0, 30.0, and 40.0,	-	(J. Prashanth, 2001)
F	-	-	600.0 and 850.0	-	(Bumjoo Kim, 2005)
F	5.5	-	-	311.2	(A. Ghosh, 2020)
C, F	-	(C) 85 to 92% (F) 85 to 94%			(B. Nath, 2017)
F	12.2	51.0	65.0 to 272.0	85.0 to 300.0	(Wirth Xenia, 2019)
	6.86		19.82		(N. Yeboah, 2013)

*Blanks indicate data not reported

2.5 Highly Porous Components in Fly Ash

SEM studies of fly ash have demonstrated the presence of high porosity/small void size components within the ash. These components most commonly include carbon particles remaining from the source coal or diatoms, which typically live in aquatic environments or are part of the source coal before combustion [27]. Diatoms are microscopic creatures that are slightly larger than bacteria, ranging from 2 to 500 micrometers in size [28]. They are unicellular organisms that are classified as Eukaryotes [28] and are one of two types of plankton called phytoplankton (*phyto* meaning plant and *plankton* meaning to drift or wander) [28, 29]. As defined by the NASA earth observatory, "phytoplankton are microscopic organisms that live in watery environments, both salty and fresh" [29]. Phytoplankton are described as microalgae as they require sunlight for reproduction and survival [30].

Due to this requirement of sunlight and aquatic environments, phytoplankton contain a buoyancy that allows them to float in the upper surface of bodies of water to obtain sunlight [30]. Along with sunlight and water, "phytoplankton also require inorganic nutrients such as nitrates, phosphates, and sulfur which they convert into proteins, fats, and carbohydrates" [30]. The second type of phytoplankton is called a dinoflagellate, which rely on a whiplike-tail called a flagella to navigate through aquatic environments that are more sustainable for their ideal living conditions [30]. They are like diatoms in that they are covered with complex shells, but the main difference, besides the tail, is that diatoms are made of a different substance [30]. In fact, diatoms are made up of a rigid silica-based structure composed of interlocking components that make up their internal porous network [30]. However, instead of relying on flagella for movement, diatoms rely on ocean currents

[30]. While residual diatoms are believed to come in part from the source coal, some field disposal conditions may support their growth in ponded ash as well.

The porous structure of diatoms results from their complex silica-based shells, with interlocking components in their inner structure [30], which resembles a sponge. The geometrical shape of the diatoms has a network of internally connected pores in addition to their outside surrounding external pore openings. The diatom's structure includes protoplasm which is closed off and protected by an outer shell armor [27, 28], known as a hydrated amorphous silica cell wall, which is denoted as the diatom's frustule [27]. These frustules encapsulate the cytoplasm of the diatom in silica, providing essentially an armor of protection for the diatom [28]. These frustules are similar to quartz and glass with densities measured from $2.1 - 2.3 \frac{kg}{m^3}$ [31].

Hamm (2003) performed a series of tests studying the stress distribution within a diatom using the finite element method and testing the compressive strength using a glass needle probe that applied pressure on four typical diatoms [31] (Figure 9). Single diatoms with diameters ranging from 50 to 100 μm required between 20 and 700 micro-Newtons (μN) of force to produce fracture [32], which was primarily due to the compressive strength of the valve and girdle band of a pennate diatom, and ranged from 330 to 680 MPa, while the Young's modulus of a typical frustule was approximately 22.4 GPa [31]. Because diatoms exhiibit a typically short lived lifespan in unideal conditions, most diatoms encountered in fly ash are not living organisms [28].

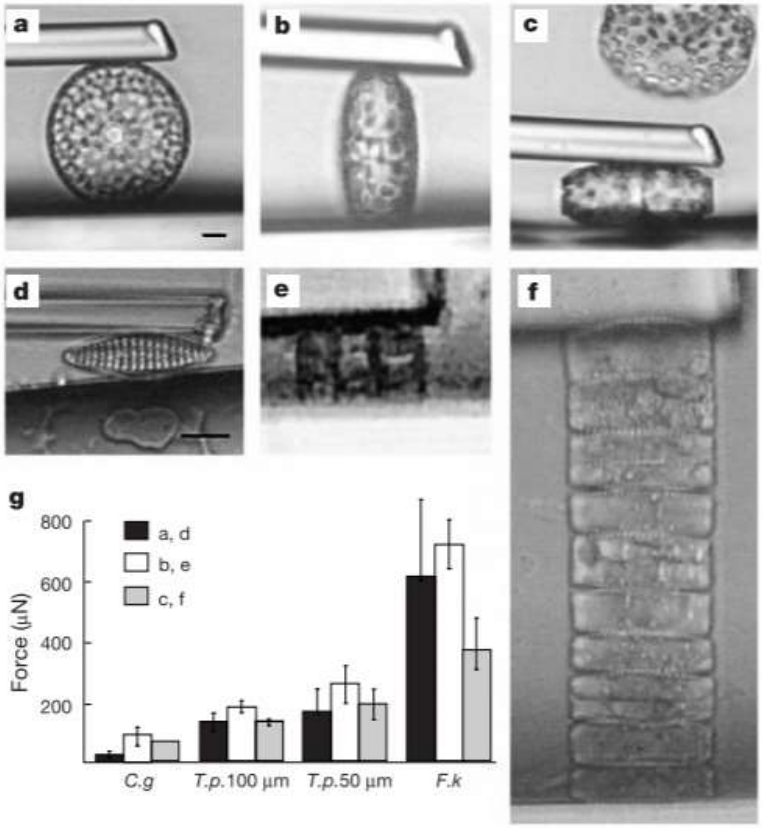

Figure 9: Hamm's needle stress distribution test (Figure from [32]).

The porous nature of a diatom results from the internal structures that are known as the hypotheca and epitheca, with each half consisting of a girdle band, mantle, and valve (Figure 10) [31, 33]. The girdle band and mantle are not as functional as the valve components. The valve components are essentially the entry and exit pores to the internal pore structure inside the diatoms. The two valves join to form an array of entry pores, displaced into patterns that are specific to the species of diatoms.

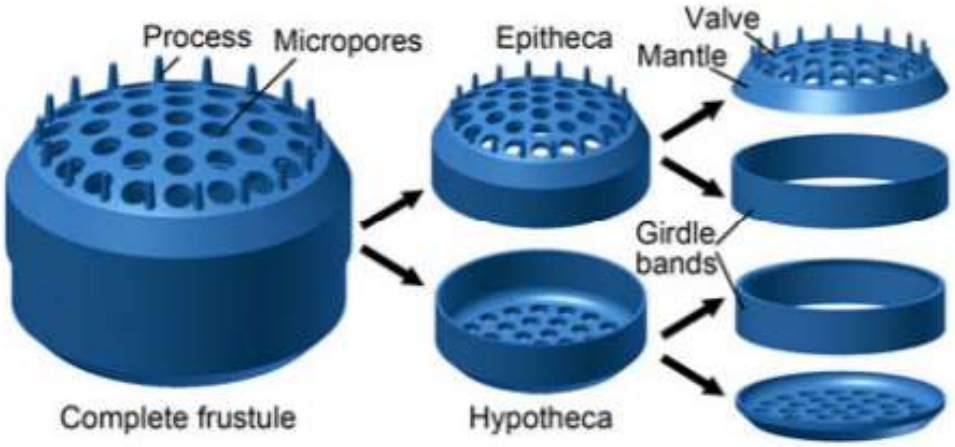

Figure 10: Diatom frustule breakdown (Figure from [31]).

Because there are over 100,000 known species of diatoms [34], they are generalized into three primary shape categories for simplicity: flaky, rod, and 3D shaped diatoms (Figure 11) [31]. Rod shape is a diatom with an elongated cylindrical shape with the pattern rotating around the x-axis, flaky is a diatom with extremely low thickness in the z-axis, and 3D shaped diatoms consist of variable shapes with a minimum thickness in the diatom's z-axis due to the large size of a girdle and mantle [31] (Figure 11).

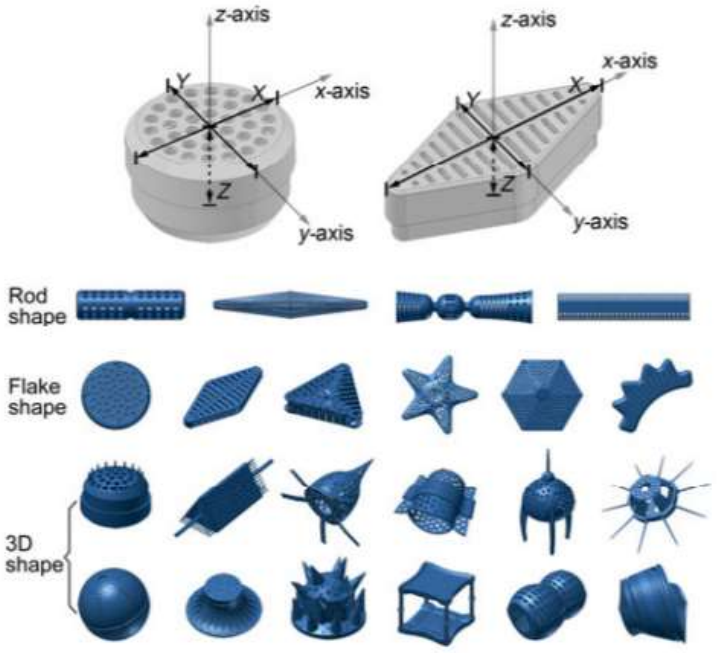

Figure 11: Categorization of diatom structures (Figure from [31]).

The multilayered pores act as substructures within the diatoms [31] which include (Figure 12): (a) a layer of large entry pores; (b) foramen pores: regularly arrayed to one half of the frustules; either hexagonal or circular chambers named areola are then layered beneath the foramen; followed by a collection of second layered pores known as blind holes with diameters of 200 nm located to the bottom of areolae; and lastly (c) sieve pores with diameter 40 nm that are spread out with each second layer pore [31]. The girdle and mantle of Coscinodiscus shows a plethora of pores with 100 nm diameters (d) [31]. These multilayered pores are the valve networks discussed in earlier sections, and with multiple layers of pores making up the substructures of these highly porous 3D diatoms, these tiny creatures present a real potential for holding, storing, or clogging the drainage networks of

the fly ash material. The highly porous nature of diatoms can most certainly alter the mean pore size average of a fly ash material.

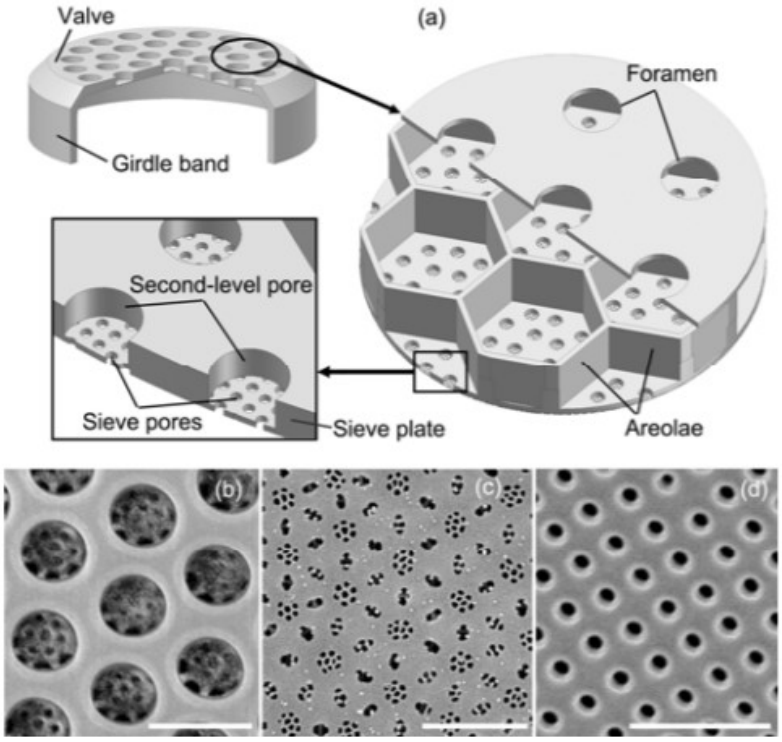

Figure 12: Multilayer internal porous structure (Figure from [31]).

Diatomaceous earth (DE) is a commercial material consisting of high concentration, fossilized silica-based frustules of diatoms [35]. Over prolonged periods of time, these fossilized diatoms accumulate in aquatic environments including sedimentary deposits within rivers, lakes, oceans, and streams [35], where they can cement into an off-white porous sedimentary rock made up of the fossilized diatom shells [35]. After these diatoms become cemented, the material is denoted as diatomite [35]. These deposits are found all over the world, with the largest deposit in the world located in California with beds 300 m (1000 feet) thick and extend over many hectares [35]. The texture of the

deposits ranges from compact rock to soft earth, can form in fresh or saltwater environments, with variable structure that is a function of the formation environment. The accumulation of diatoms can create large deposits over time, and demonstrate the significant growth rate of diatoms in aquatic environments, including CCP ash ponds.

In addition to deposits of diatoms, fly ash frequently contains large quantities of partially combusted carbon, similar to an activated carbon phase. Normally, the activation in the term "activated carbon" comes from the selective industrial gasification of the carbon atoms for thermal activation and secondly from the use of phosphoric acid during chemical activation [36]. Activated carbons can be made from various materials such as hard woods, fruit stones, coconut shell, and synthetic macromolecular systems [36].

The carbon particles found in coal fly ash and activated carbon are highly porous and consist of essentially empty space that is encased in a structure of carbon atoms [36], and can be described "as a crude form of graphite with a random or amorphous structure, which is highly porous over a broad range of pore sizes" [37]. Activated carbon structures are remnants of the original carbon sources, with macropores (diameters that are larger than 50 nm), mesopores (diameters between 2 and 50 nm), and micropores (diameters less than 2 nm) [37]. In terms of the distribution of pores, micropores normally account for the majority of the specific surface area of a porous carbon particle [37], and the macro and mesopores act as the entry pores for the porous carbon particles. Within the internal surface area of the carbon structure, there is a dense network of highly porous micropores [37]. SEM images of the carbon particles found in coal and biomass ash demonstrate a variety of structures (Figure 13).

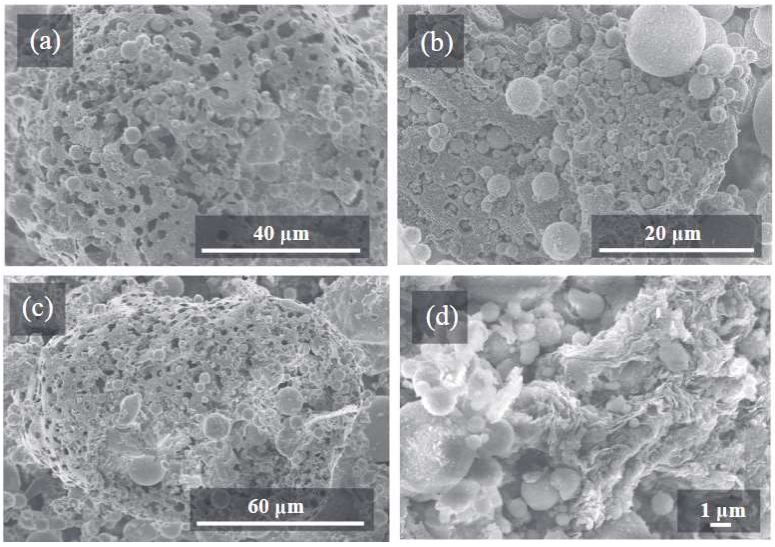

Figure 13: Four SEM images of carbon particles from ponded fly ash (Figure from [38]).

In contrast to fly ash, activated carbon is a highly processed material typically developed for application as sorbents, and can be produced in granular, pelletized, or powder form [39]. For activated carbon produced from coal, the raw coal is ground, placed into a binder, and then mixed into a paste, placed under pressure, and granulated into pellets [39]. Carbonation of the pellets occurs as they are heated at temperatures from 500°C to 600°C, followed by an activation of the pellets at 900°C to 950°C [39].

CHAPTER 3 MATERIALS AND METHODS

In this work, a series of experiments were performed to quantify the impact of highly porous components (AC or DE) mixed in to a low surface area particulate media matrix. While the topic of investigation was to gain insight into the hydraulic conductivity of fly ash mixtures, these experiments were performed using F110 sand as the inert porous media, while mixing in increasing percentages of the highly porous activated carbon or diatomaceous earth (up to 10.0% by volume). Sand was chosen as the matrix material for several reasons: it is chemically inert and nonreactive, it has rounded or sub-rounded (or approximately spherical) shape, and the hydraulic conductivity experiments could be performed in a relatively short duration. Details of the materials and methods used in the experimentation are given in the following sections.

3.1 Materials

The inert porous media chosen for study was F110 sand, which was obtained from US Silica and was used as received. Coal-derived activated carbon granules (Carbon Resources CR2050B) were obtained from (*Carbon Activated Corp)* [22] and diatomaceous earth was obtained from two sources: Earthborn Elements and Diatomaceous Earth LLC (*diatomaceousearth.com)*, both of which distribute diatomite mined in the United States for a wide variety of applications, ranging from health to landscaping. Freshwater diatoms were tested in this study (Appendix A) contains reference table for basic properties of DE tested). Both AC and DE were used as received. Silica beads were obtained from (*BioSpec*

Products) in sizes 1.0 mm, 0.5mm, 0.25 mm, and 0.1mm in diameter and were used for SEM Calibration.

3.2 Methods

Initially in the experimental planning phase, glass silica beads were investigated as the inert porous media component for hydraulic conductivity testing. A scanning electron microscope (Hitachi SU8010) was used to visually inspect the porous media tested in this study for consistency in shape, particle diameter, pits, and cracks. Samples were prepared by placing the particles on to carbon tape sample plates (Figure 14), after which the samples were placed into a sputterer (Q-150 T ES) under applied vacuum, where thin layers ($< 30\ nm\ thin$) of gold and carbon coatings were applied to the surface of the particles to obtain better resolution under SEM imaging. Processed images are shown in Appendix B. Although the silica beads were not used for hydraulic conductivity testing, the obtained SEM images were used for calibration and as references for additional sample imaging. The same process of SEM imaging was used for the base material sand (F110), and highly porous components (DE and AC) (Figure 15).

Figure 14: Glass silica beads (*BioSpec Products*), from left to right: 1 mm, 0.5 mm, and 0.25 mm.

Figure 15: Carbon sample plates for Ottawa F110 sand, coal-based AC, and DE.

SEM imaging of DE sample 1 was time consuming, requiring approximately four hours to locate fully intact diatoms due to the presence of what appeared to be mostly crushed and damaged diatom structures (Figure 16 and Figure 17). Only one diatom was found with a fully intact structure. The second viewing of this sample took multiple hours without locating a single fully intact structure.

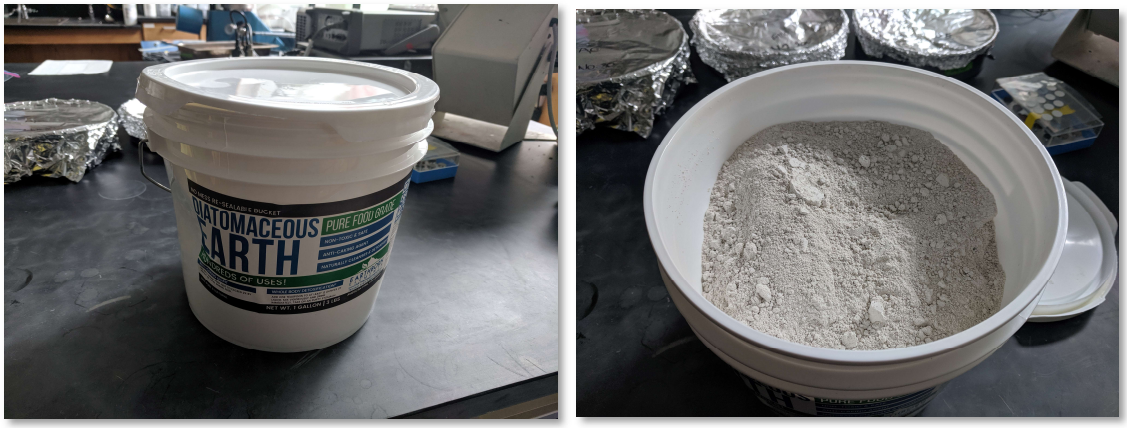

Figure 16: Diatomaceous earth (Sample Number 1).

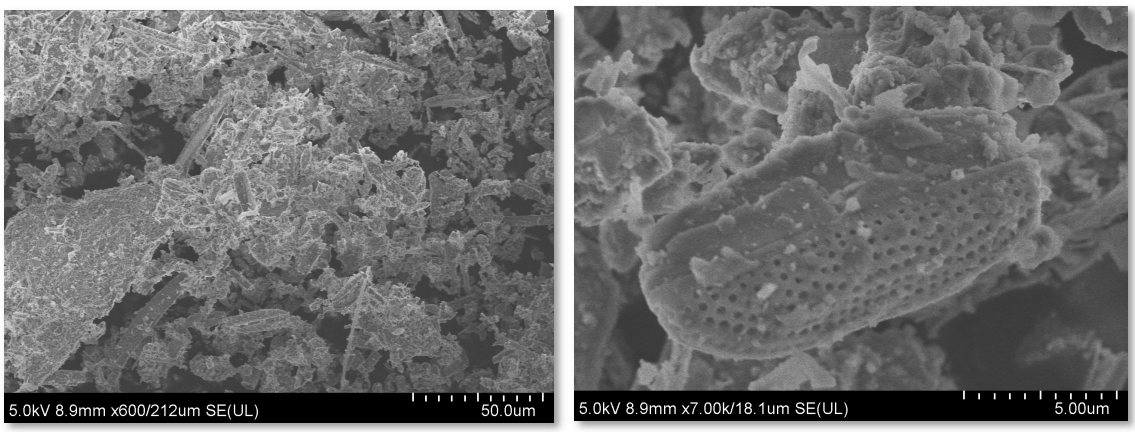

Figure 17: SEM image of diatomaceous earth (Sample Number 1).

A food grade sample of diatomaceous earth, specified as 100% diatomaceous earth, with minimal processing or crushing proved more robust, with multiple intact diatoms clearly visible through SEM imaging (Figure 18 and Figure 19).

Figure 18: Diatomaceous earth (Sample Number 2).

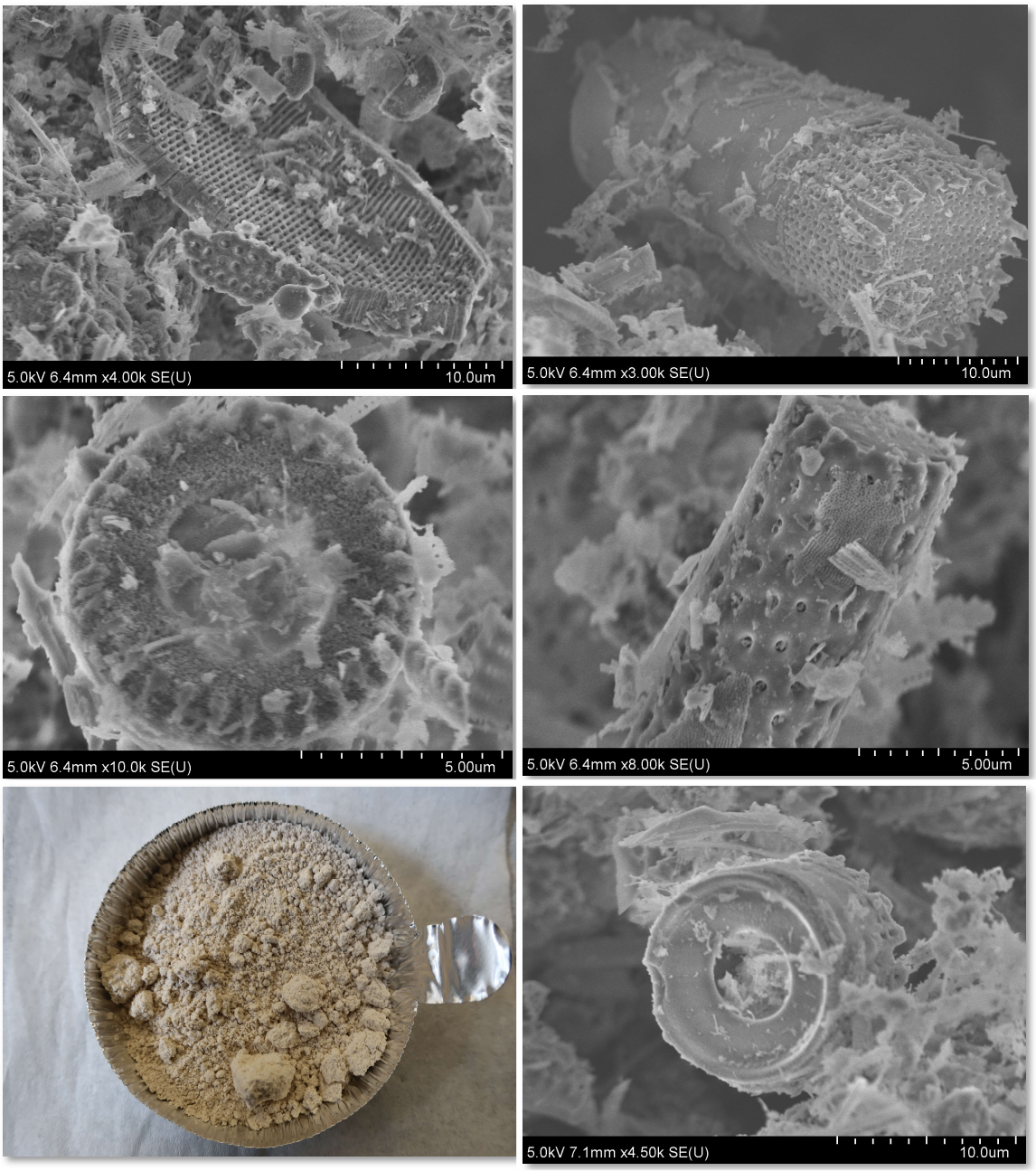

Figure 19: SEM image of diatomaceous earth (Sample Number 2).

The range of particle sizes in the activated carbon posed challenges for imaging. Consequently, a small percentage of particles were separated for imaging by performing an intial sieve analysis of the material through a No. 20 sieve (in accordance with ASTM

standard sizing). The finer grained particles that passed the No. 20 sieve were then imaged in the SEM (Figure 20). SEM imaging confirmed that the activated carbon was a highly porous carbon structure, as anticipated. The SEM images of Ottawa F110 Sand (sieved through No. 70 sieve) showed subangular grains (Figure 21).

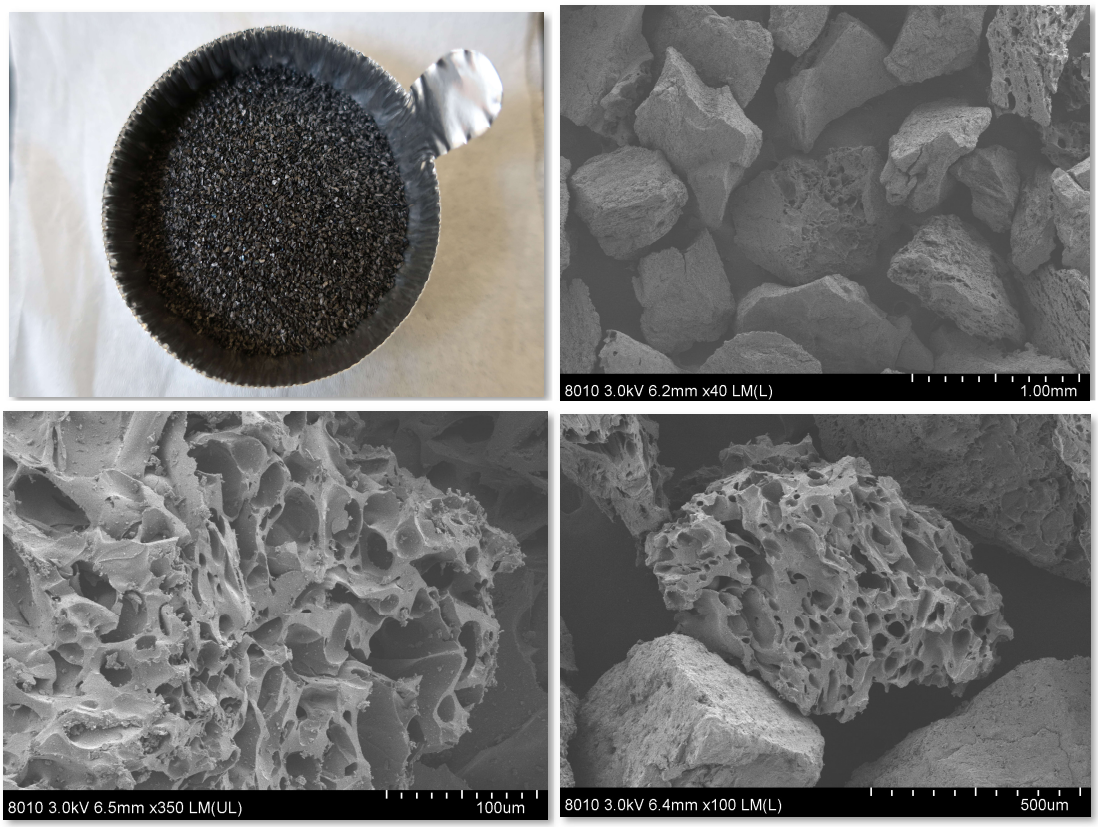

Figure 20. Photo and SEM images of activated carbon.

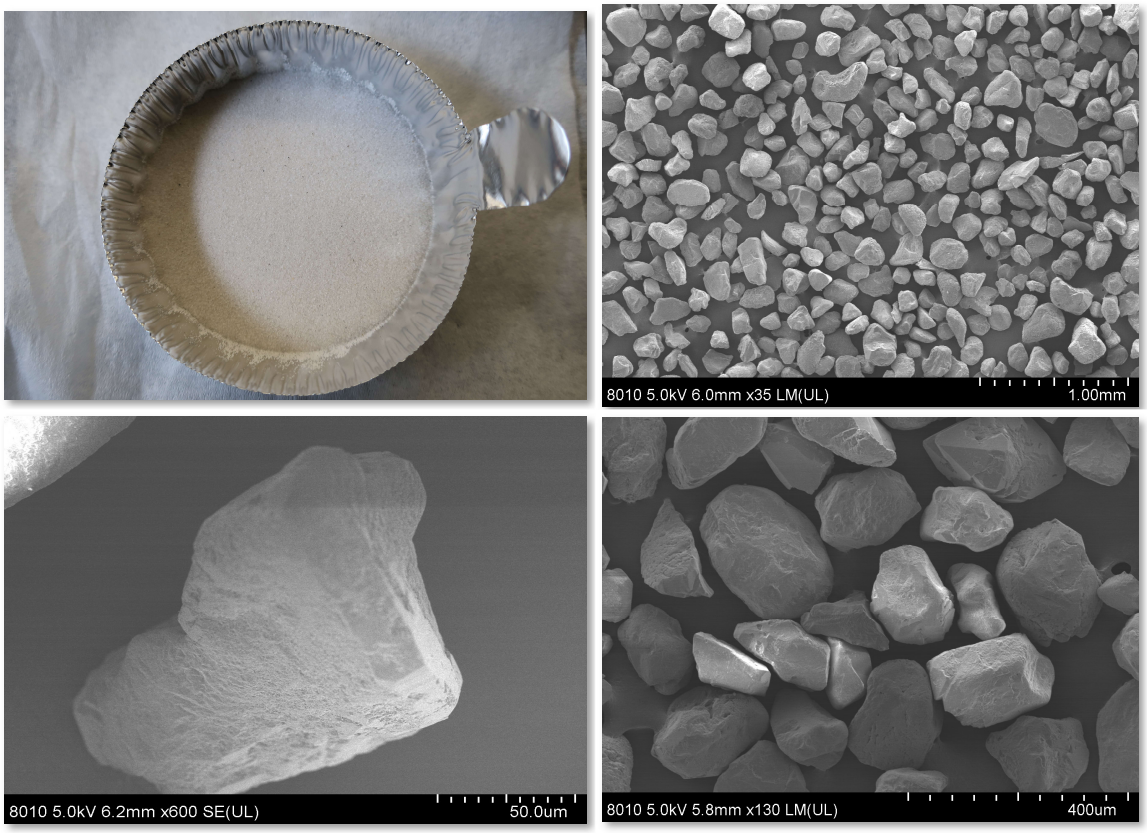

Figure 21. Photo and SEM images of F110 sand.

The grain size distributions of the particles were measured using sieve analysis for both the sand and the activated carbon according to ASTM D422. Grain size distributions for F110 sand were controlled by sieving through a No. 70 sieve to separate the finer grains from the distribution (Figure 22). The grain size distribution for activated carbon was performed in the as received condition with no sieving (Figure 23). The median grain diameter was 0.135 mm for the sand and 0.68 mm for the activated carbon (Table 4). Chemical analysis for the sand was provided by US Silica (Table 5). The minimum and maximum void ratios of the sand were measured using the methods described in ASTM D4253 and ASTM D4254. Methods 1A and C were used, respectively. Note that the

activated carbon particles were not filling void space in the mixture as they were larger than the sand particles.

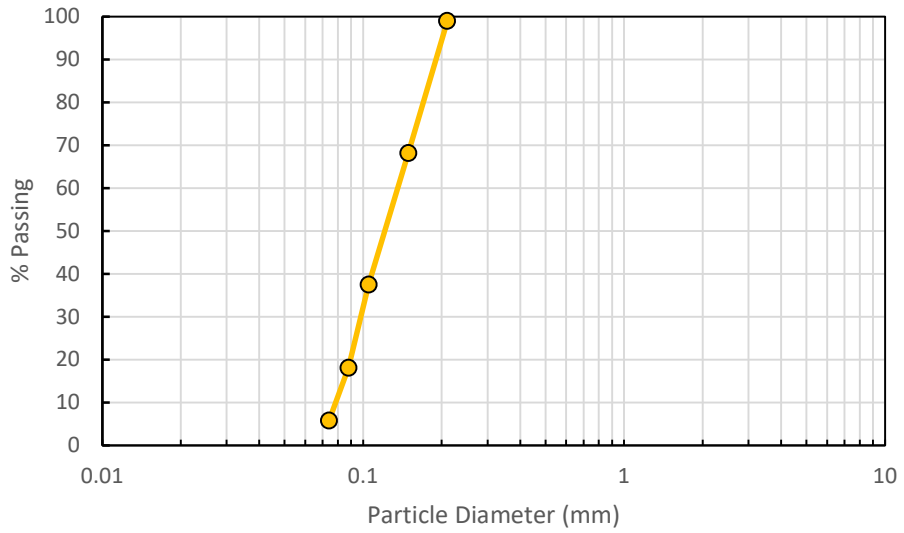

Figure 22: Grain size distribution for F110 sand sieved through No. 70 sieve.

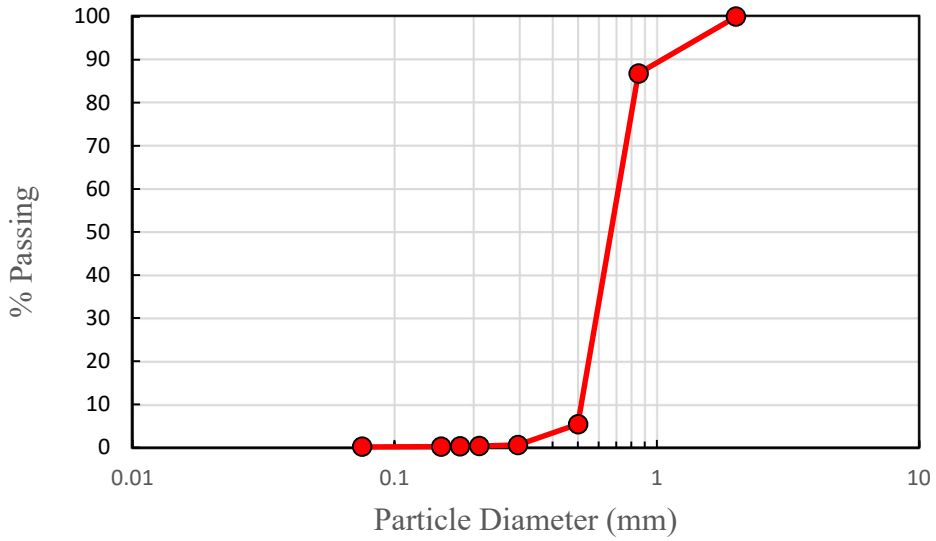

Figure 23: Grain size distribution for activated carbon (unsieved).

Table 4: Material Properties of Base Materials and Mixtures

Material	D_{50} (mm)	C_u	C_c	e_{max}	e_{min}
F110	0.135	1.88	0.83	0.84	0.55
Activated	0.68	1.4	1.03	-	-
Diatomaceous	0.0144	0.914	1.08	-	-

Table 5: Chemical Analysis of F110 Sand

	Chemical Analysis (%)
SiO_2 (Silicon Dioxide)	99.8
Fe_2O_3 (Iron Oxide)	0.020
Al_2O_3 (Aluminum Oxide)	0.060
TiO_2 (Titanium Dioxide)	0.010
CaO (Calcium Oxide)	< 0.01
MgO (Magnesium Oxide)	< 0.01
Na_2O (Sodium Oxide)	< 0.01
K_2O (Potassium Oxide)	< 0.01
LOI (Loss On Ignition)	0.01

The grain size distribution of diatomaceous earth was measured by laser diffraction using a particle size analyzer (Malvern 3000 Hydro EV). Five tests (each with 5 measurements for a total of 25 measurements on 1 sample of diatomaceous earth) were performed. The tests were designed to see the effects that ultra sound create when applied from zero ultra sound with an increasing increment of 30 additional seconds of ultrasound

(US) to each test (DE (1-5) - 0sUS, DE (6 - 10) - 30sUS, DE (11 - 15) - 60sUS, DE (16 - 20) - 90sUS, DE (21 - 25) - 120sUS). This proved to have a subtle decrease in D_{10}, D_{50}, and D_{90} (Table 6). This decrease occurs because additional amounts of ultrasound result in more effective removal of particles that clump together and go on to provide a more accurate measurement of individual DE particles (Note that the diatom distribution is given as cumulative percent volume as a function of particle size in micrometers (Figure 24)). Being set up in 5 tests possibly creates a spike of abnormal values at the start of 3 out of 5 of the tests. It is not well understood for these to be abnormally sized particles in the DE, as they typically range from 2 to 500 μm [28]. However, the possibility does exist that a few particles stay clumped together even after ultrasound is applied in the tests. These abnormalities are included in the final averaged measurements. The resulted averaged D_{50} of the diatomaceous earth is 14.4 μm (Figure 24 and Table 6).

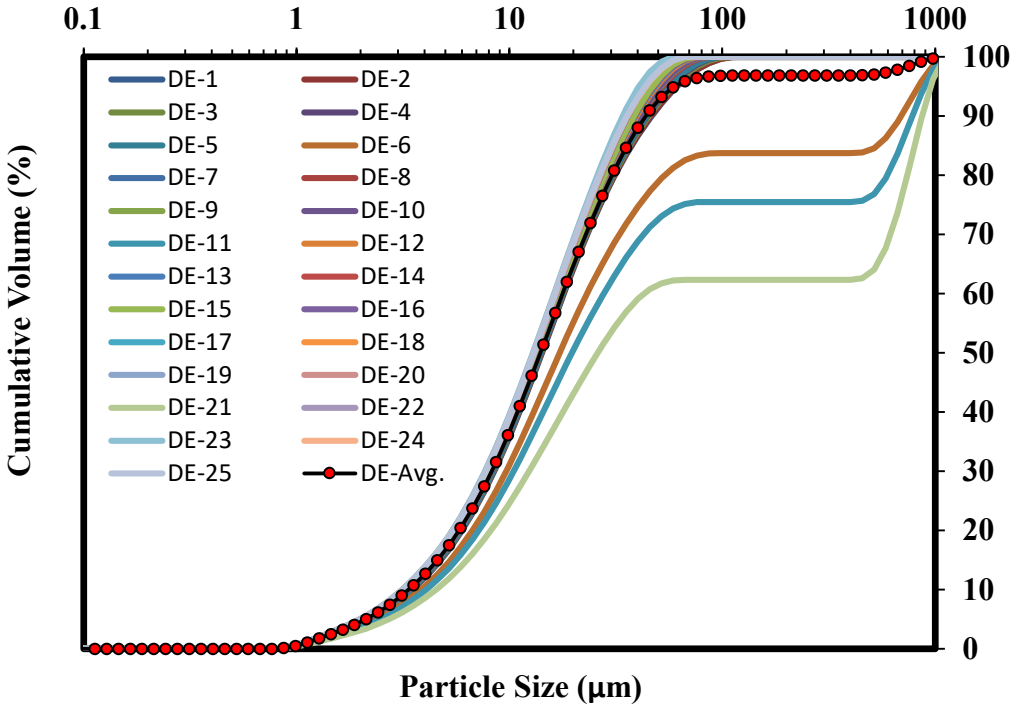

Figure 24: Grain size distribution for diatomaceous earth measured using laser diffraction.

Table 6: D_{10}, D_{50}, and D_{90} values for DE Measured with Laser Diffraction

Sample	D_{10} (µm)	D_{50} (µm)	D_{90} (µm)
DE-1	3.49	14.2	46.6
DE-2	3.47	14.2	46.2
DE-3	3.46	14.1	45.2
DE-4	3.44	14	44.4
DE-5	3.43	14	43.9
DE-6	3.84	17.2	692
DE-7	3.36	13.7	42.1
DE-8	3.36	13.7	41.6
DE-9	3.35	13.7	41.2
DE-10	3.35	13.7	41
DE-11	4.06	19.7	782
DE-12	3.29	13.5	39.6
DE-13	3.28	13.5	39.1
DE-14	3.27	13.4	38.7
DE-15	3.27	13.4	38.5
DE-16	3.2	13.1	36
DE-17	3.2	13.1	35.8
DE-18	3.2	13.1	35.5
DE-19	3.2	13.1	35.4
DE-20	3.2	13.1	35.8
DE-21	4.52	26	868
DE-22	3.15	13	34.8
DE-23	3.14	12.9	34.1
DE-24	3.16	13	35.8
DE-25	3.16	13	35.6
Average	**3.39**	**14.4**	**128**
St. Dev.	0.318	2.84	247

The specific gravities (G_s) of the F110 sand, activated carbon, and diatomaceous earth were measured in triplicate (minimum) according to ASTM D854 (pycnometer method) (Table 7). All measured values were reasonable and within expected ranges of the specific gravity for each material tested.

Table 7: Specific Gravity for F110 sand, DE, and AC materials

	A	B	C	D	Avg G_s	St Dev
F110 Sand	2.674	2.660	2.664	-	2.67	0.0067
Diatomaceous Earth	2.274	2.256	2.208	2.201	2.23	0.034
Activated Carbon	1.874	1.865	1.859	-	1.87	0.0076

Mixtures of the three materials were created by blending the highly porous material (either AC or DE) at a given percentage by volume with the remaining percent volume occupied by F110 sand. A sample calculation for volume/mass determination is provided in Appendix C. Mixtures were blended by hand and were then used as the source material for subsequent testing. The blended materials were tested for limiting void ratios (e_{max}, e_{min}) and hydraulic conductivity according to the volume proportions (Table 8).

Table 8: Volume Proportions for Tested Mixtures

Sand % (% Volume)	Porous Additive AC or DE (% Volume)	e_{max} with DE	e_{min} With DE	e_{max} with AC	e_{min} With AC
100	0	0.84	0.55	0.84	0.55
97.5	2.5	0.95	0.58	0.88	0.58
95.0	5.0	1.02	0.59	0.92	0.62
90.0	10.0	1.37	0.59	0.98	0.68

Hydraulic conductivity tests were performed according to ASTM D5084-16a, using the flexible wall permeability test with constant head (method A). The sample being tested was confined with a latex membrane with confining pressures ranging from 7 to 69 kPa (1 to 10 psi). Specimens were saturated by flow under gravity head from the pressure panel, with inflow at the top of the sample and outflow at the bottom of the sample. Saturation flow was continued until B values measured a minimum of 0.95.

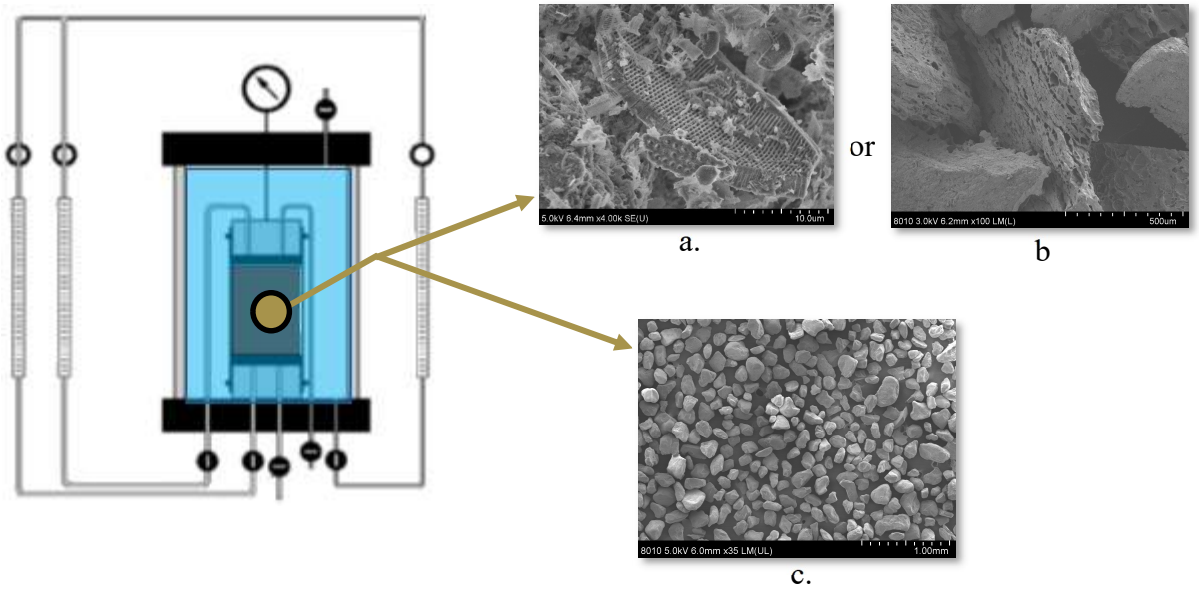

Figure 25 : Hydraulic Conductivity Setup displaying SEM of highly porous and isolated components (Diatomaceous Earth (a.-10 μm scale) or Activated Carbon (b.-500μm $scale$)) to be placed into base material (F110 sand (c.-1 mm scale)), figure taken from ASTM D5084-16a Standard for Permeability Testing.

During this study, the following characterization tests were performed on base materials (Sand, DE, and AC) in order to develop properly controlled volume percentage-based blends for the series of hydraulic conductivity tests. These tests were performed on the fine sand (F110) mixed with increasing percentages of each additive (Table 9).

Table 9: Summary of Characterization and Hydraulic Conductivity Tests Performed using Sand/Porous Mixtures

Soil	Characterization Tests	Hydraulic Conductivity Tests
100% sand	SEM Grain size (sieve) Limiting void ratios Specific gravity	2
100% DE	SEM Grain size (laser diff) Specific gravity	0
100% AC	SEM Grain size (sieve) Specific gravity	0
97.5% sand/2.5% DE	Limiting void ratios	2
95.0% sand/5.0% DE	Limiting void ratios	2
90.0% sand/10.0% DE	Limiting void ratios	2
97.5% sand/2.5% AC	Limiting void ratios	1
95.0% sand/5.0% AC	Limiting void ratios	1
90.0% sand/10.0% AC	Limiting void ratios	1

CHAPTER 4 RESULTS AND DISCUSSION

4.1 Results

The sand/porous admixture samples were tested for limiting void ratios, relative density, and hydraulic conductivity, with the goal of identifying the effects of the simulated porous components (diatomaceous earth and activated carbon) have on the hydraulic conductivity of F110. The components were added to sieved F110 sand, and samples were tested at 2.5%, 5.0%, and 10.0% by volume addition to the mixture.

4.1.1 Relative Density

The blended samples (sand with 0%, 2.5%, 5.0%, or 10.0% DE or AC by volume) were each tested for limiting void ratios and relative density in accordance with ASTM D (4253 and 4254, tests performed at 60 Hz for 10 minutes each). The data showed a decrease in the density of the mixture as the volume percentage of the diatomaceous earth was increased, as was anticipated due to the lower specific gravity of the DE compared to the silica sand and to the angular nature of the DE particles (Table 10 and Figure 26). The minimum densities decreased from 1.45 g/cm^3 for F110 100% sand to 1.11 g/cm^3 for the 90.0% sand and 10.0% DE mixture. The maximum density also decreased, although the magnitude of the decrease was less pronounced (from 1.73 to 1.65 g/cm^3). The calculated e_{max} and e_{min} were inversely proportional to the density values and show positive correlation with the increasing percentages of diatomaceous earth added to the mixture with F110 sand. Similar trends were observed for mixtures made with F110 sand and activated carbon (Table 11 and Figure 27).

Table 10: Relative Density and Limiting Void Ratios for Mixtures with DE

	F110 Sand	2.5% DE	5.0% DE	10.0% DE
Minimum Density (g/cm^3)	1.45	1.36	1.31	1.11
Maximum Density (g/cm^3)	1.73	1.68	1.66	1.65
e_{max}	0.84	0.95	1.02	1.37
e_{min}	0.55	0.58	0.59	0.59

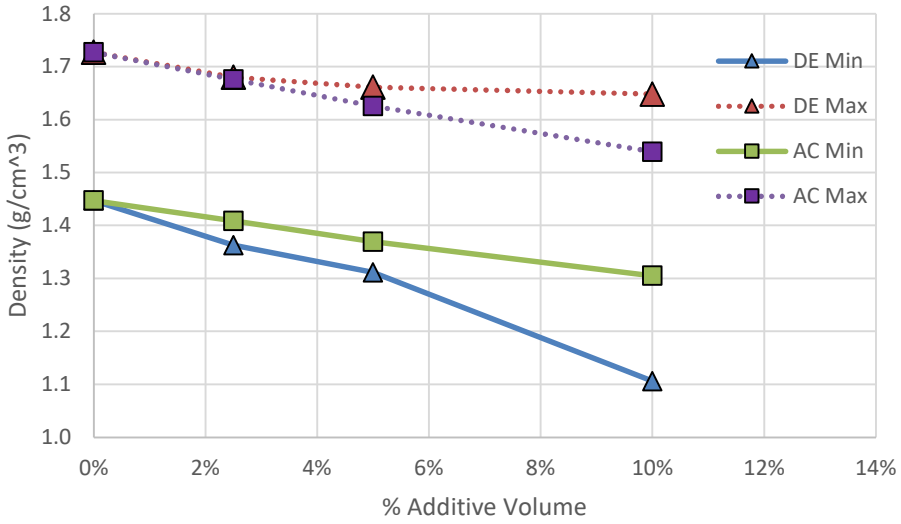

Figure 26: Density as a function of percent DE or AC in mixture with F110 sand.

Table 11: Relative Density and Limiting Void Ratios for Mixtures with AC

	F110 Sand	2.5% AC	5.0% AC	10.0% AC
Minimum Density (g/cm^3)	1.45	1.41	1.37	1.31
Maximum Density (g/cm^3)	1.73	1.68	1.63	1.54
e_{max}	0.84	0.88	0.92	0.98
e_{min}	0.55	0.58	0.62	0.68

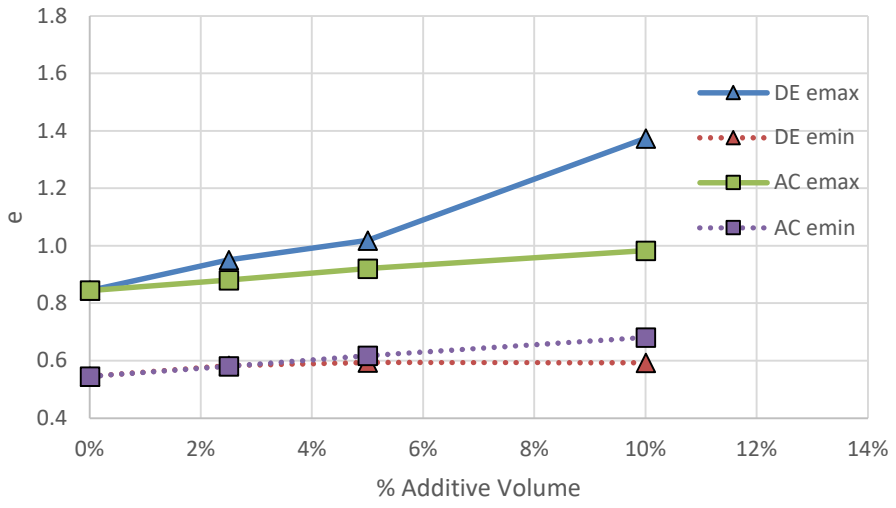

Figure 27. Limiting void ratios as a function of percent DE or AC in mixture with F110 sand.

The correlations of decreasing densities were directly related to the % additive volumes of diatomaceous earth and activated carbon. However, when comparing the effect of diatomaceous earth and activated carbon on the mixture densities and void ratios, the data demonstrated that the diatomaceous earth had a more significant impact on the fabric and particle packing than did the activated carbon samples in the minimum density tests. For

minimum density, samples prepared with diatomaceous earth had a roughly 25.0% decrease in minimum density compared to a 10.0% decrease in minimum density for mixtures made with activated carbon. For maximum densities, the DE mixtures showed a 5.0% decrease in maximum density as the volume of DE in the mixture was increased to 10.0%, while the maximum densities of mixtures made with activated carbon, decreased roughly 10.0% over the same scale.

4.1.2 Hydraulic Conductivity Tests

F110 Sand

Two hydraulic conductivity tests were performed using 100% Ottawa F110 sand (sieved) in accordance with ASTM D5084-16A (Figure 28). The samples were prepared at a relative density of 40.0%, and saturated until a B value of 0.95 was achieved. Hydraulic conductivity was tested at confining pressures ranging from 14.8 kPa (2 psi) to 75.8 kPa (11 psi), in increasing increments of 6.9 kPa (1 psi) with each test having a gradient of 6.9 kPa (1 psi) between inlet / outlet pressures for both tests. The measured hydraulic conductivity ranged from 1.8×10^{-3} cm/sec at the lowest confining pressure to 1.3×10^{-3} cm/sec for sample No.1 and 9.3×10^{-4} cm/sec for sample No.2 at the highest confining pressure.

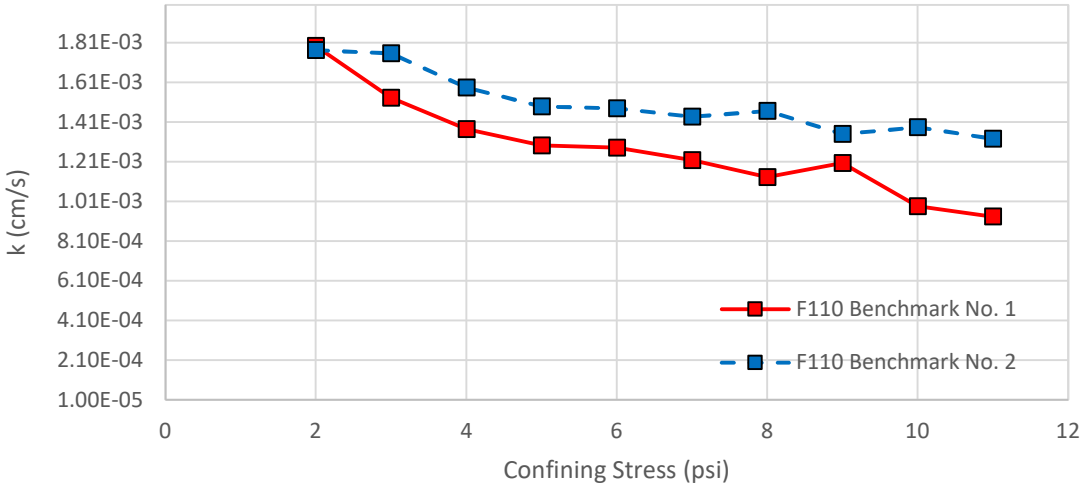

Figure 28: Hydraulic conductivity test results for 100% Ottawa F110 sand (40.0% D_R).

Mixtures with Diatomaceous Earth and Activated Carbon

Mixture samples were prepared for hydraulic conductivity testing with both DE and AC. For the DE mixtures, the sample relative densities ranged from 53.0 to 61.0%, and were reasonably close to the target relative density of 60.0% for the blends (Figure 30). In contrast, samples prepared with the activated carbon mixture ranged from a relative density of 60 to 89.0%, maintaining an almost uniform density as a function of additive percentage (Figure 29), and increasing by about 30.0% in the tested mixtures (Figure 31). Both blends increased in relative densities as percent additive increased because the addition of more material to each blend changed the fabric of the mixture and impacted the limiting void ratios. As new material was added to each blend, the e_{max} increased; however, the AC mixtures increased in relative density at a much faster rate of increase than the DE mixtures. A consistent method of control and compaction was used in all of the experimental preparations, with control of the mixing processes, volume percentage, and compaction

method. The target relative density was 60.0% for the mixture samples, and using the same method of compaction across the preparation of the six DE samples achieved D_r values of 51.0 to 61.0%. This level of control over the relative density in DE was achieved because the DE is finer than the F110 sand, and filled the previously empty void spaces without impacting the mixture fabric significantly. In contrast, the activated carbon was composed of particles with small diameters, but also diameters much larger than the F110 sand. These larger particles occupied space without filling voids. This effect became more significant with each additional volume percentage increment added to the sample. To control this relative density, additional levels of compaction effort are required as additional percentage of activated carbon was added to the samples. In short summary, this experimental design cannot use the same level of compaction efforts to achieve the same relative density across the different percentage of activated carbon components. The significance of the rate at which relative density increases within activated carbon samples was not accounted for during the procedure, which resulted in an almost 30.0% difference in relative density control between the 2.5% and 10.0% activated carbon samples.

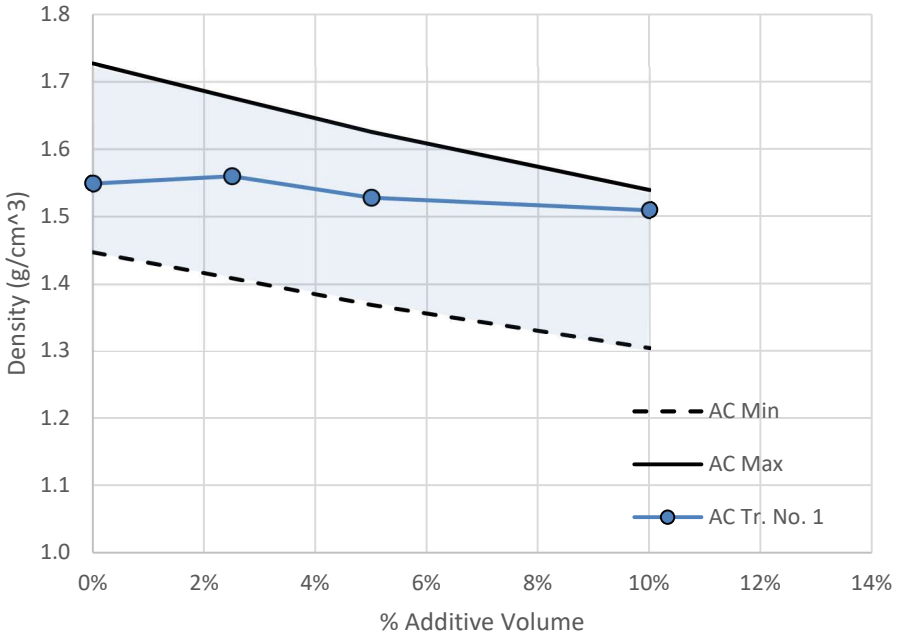

Figure 29: Density of AC mixture specimens prepared for hydraulic conductivity testing as a function of additive volume.

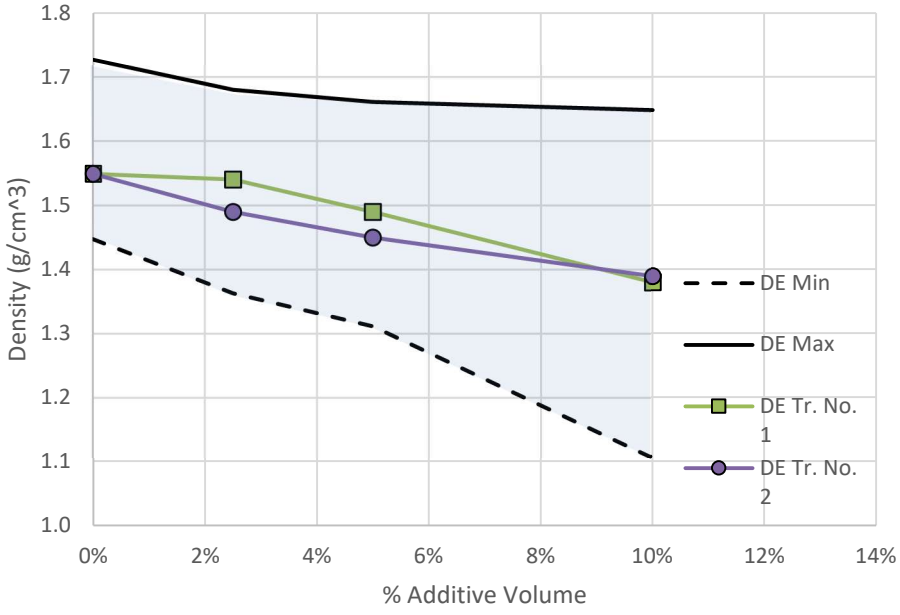

Figure 30: Density of DE mixture specimens prepared for hydraulic conductivity testing as a function of additive volume.

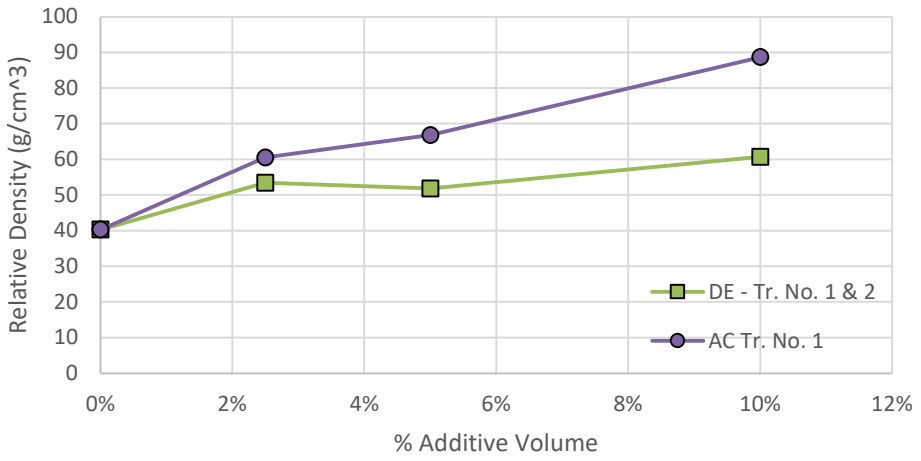

Figure 31: Relative density of DE and AC as a function of % additive volume.

The specimens for hydraulic conductivity were prepared with additive volumes of 2.5%, 5.0%, and 10.0%, and were tested at confining stresses of 6.9 kPa to 69.0 kPa (1 to 10 psi), in increasing 6.9 kPa (1 psi) increments with each test also having a gradient between inlet / outlet pressures of 6.9 kPa (1 psi). Samples were saturated until a minimum a B-value of 0.95 was achieved. After achieving the minimum required B-value, the hydraulic conductivity tests were performed immediately. The hydraulic conductivity specimens tested with mixtures 2.5% DE / 97.5% sand had a D_r of 53.0% (averaged between (D_r) 61.0%, (first trial) and (D_r) 46.0% (second trial)) (Figure 32 and Table 12).

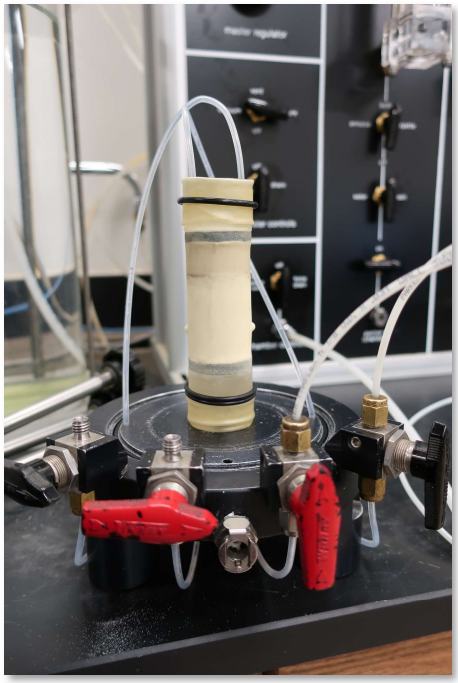

Figure 32: Photo of 2.5% DE sample set up under vacuum before saturation. All mixture specimens were tested with the same preparation methods.

Table 12: Relative Densities and Photos of Tested DE Mixtures

Mixture (%)	**Relative Density (%)**	**Wet Soil Image**	**Dry Soil Image**
97.5% sand / 2.5% DE	53	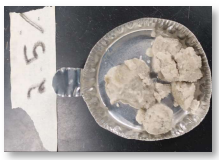	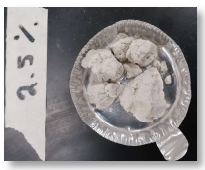
95.0% sand / 5.0% DE	52	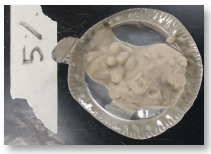	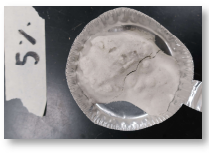
90.0% sand / 10.0% DE	61	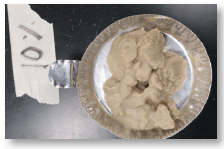	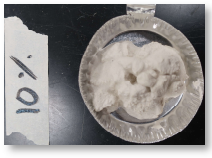

For the two samples prepared with 2.5% diatomaceous earth, the measured hydraulic conductivity values were sensitive to relative density, with the first sample prepared at a relative density of roughly 61.0% measuring a magnitude of $10^{-4}\frac{cm}{s}$, while the second sample was prepared at a relative density of roughly 46.0% measured at a magnitude of $10^{-5}\frac{cm}{s}$. The higher relative density sample was more sensitive to confining stress, with conductivity values decreasing by a factor of 2 (from $2.6\,x\,10^{-4}\frac{cm}{s}$ to $1.3\,x\,10^{-4}\frac{cm}{s}$) as the confining stress was increased. The sample prepared at 46.0% relative density showed only slight dependence on confining stress (Figure 33).

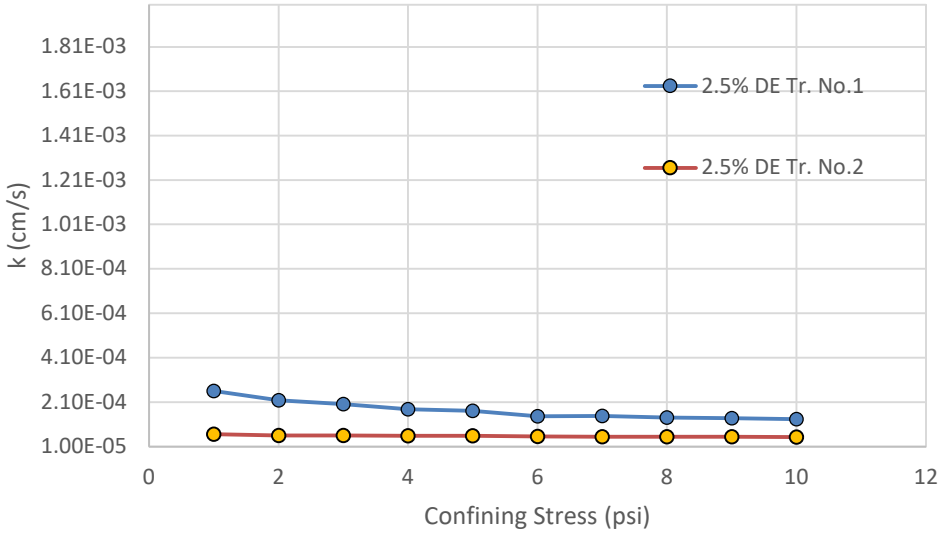

Figure 33: Hydraulic conductivity for 2.5% DE /97.5% sand mixtures as a function of confining stress and relative density.

Hydraulic conductivity tests were performed for mixtures with 5.0% DE and 95% sand at relative densities of 58.0% and 45.0% (Figure 34). Similar magnitudes of conductivity were measured for the 5.0% mixtures ($10^{-4}\frac{cm}{s}$ -$10^{-5}\frac{cm}{s}$) as were measured

for the 2.5% mixture, as well as similar sensitivity to confining stress as a function of relative density (Figure 35).

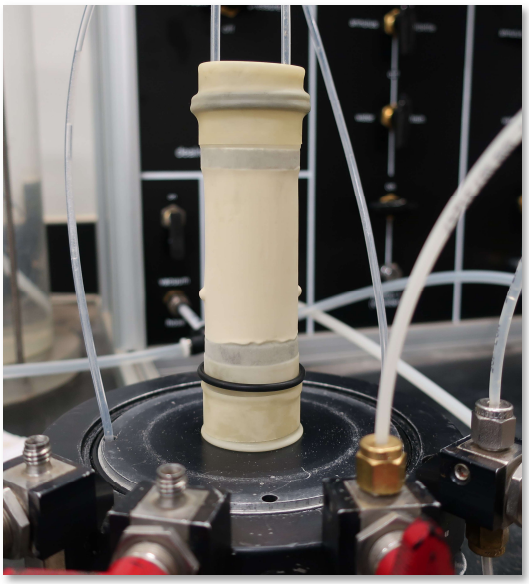

Figure 34: Photo of 5.0% DE sample set up under vacuum before saturation.

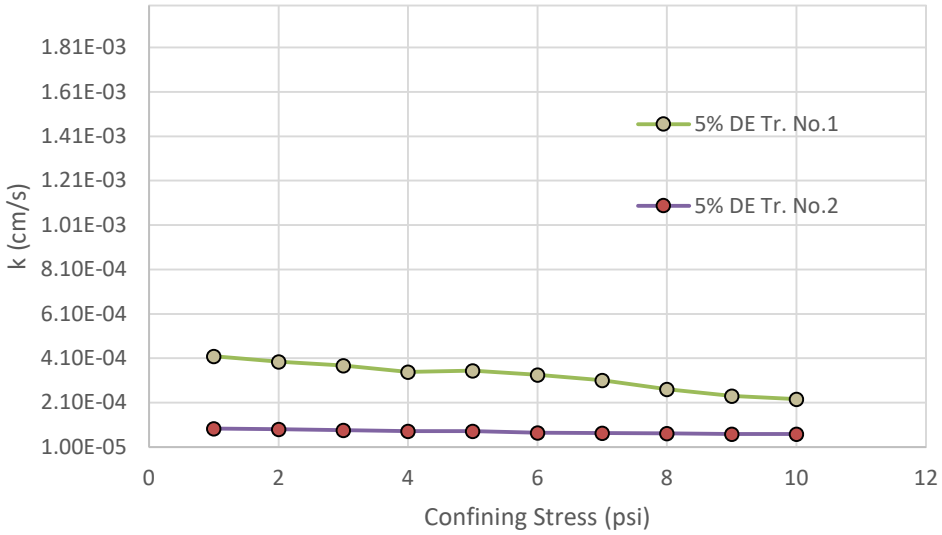

Figure 35: Hydraulic conductivity for 5.0% DE /95.0% sand mixtures as a function of confining stress and relative density.

For mixtures with 10.0% DE, the tested relative densities for the samples were 59.0%, and 61.0% (Figure 36). Targeted values for these specimens were achieved during preparation, and resulted in similar relative densities. Both tests had conductivity values on the order of magnitude of $10^{-5}\,\frac{cm}{s}$ and relatively little sensitivity to confining stress (Figure 37).

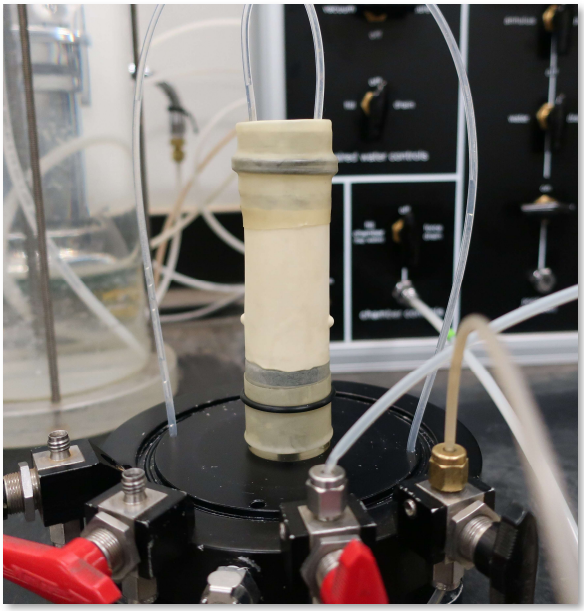

Figure 36: 10.0% DE image of sample set up under vacuum before saturation.

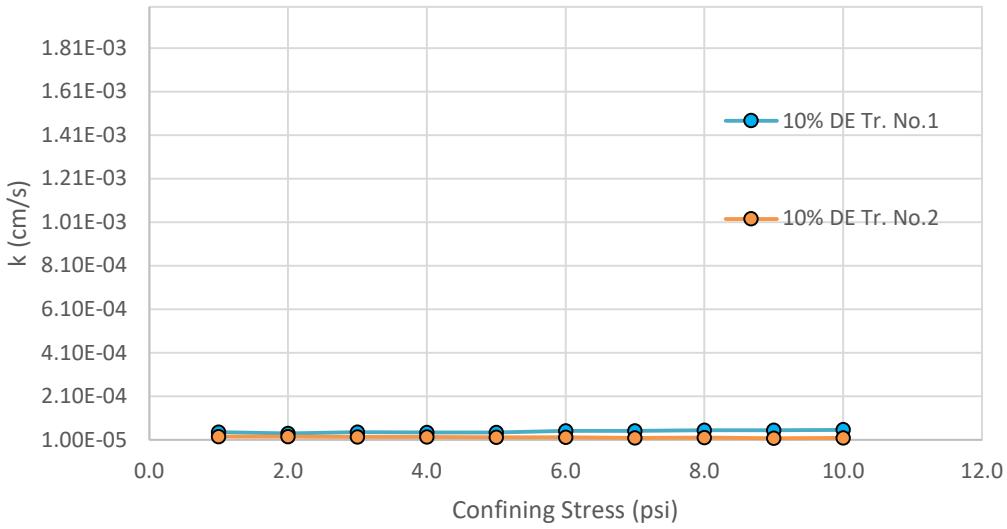

Figure 37: Hydraulic conductivity for 10.0% DE / 90.0% sand mixtures as a function of confining stress and relative density.

All tests for mixtures of AC with sand were performed in a similar manner as the DE mixtures and were saturated until the B-value reached a minimum of 0.95. Test conditions for each trial are given in the following table (Table 13) (Figure 38). The measured hydraulic conductivity ranged from $1.4\ x\ 10^{-3}\ \frac{cm}{s}$ to $9.2x\ 10^{-4}\ \frac{cm}{s}$ for the mixture with 2.5% AC; from $1.9\ x\ 10^{-3}\ \frac{cm}{s}$ to $1.3\ x\ 10^{-3}\ \frac{cm}{s}$ for the mixture with 5.0% AC; and from $7.1\ x\ 10^{-4}\ \frac{cm}{s}$ to $3.8\ x\ 10^{-4}\ \frac{cm}{s}$ for the mixture with 10.0% AC (Figure 39).

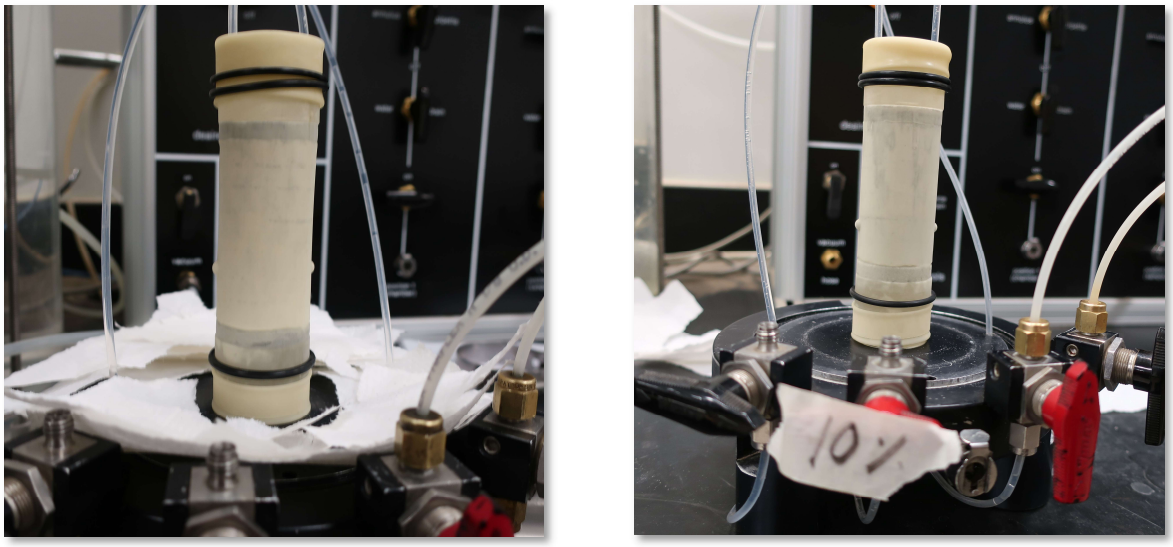

Figure 38: 2.5% (left) and 10.0% (right) AC images of sample set up under vacuum before saturation.

Table 13. Relative Densities and Photos of Tested AC Mixtures

Mixture (%)	**Relative Density (%)**	**Wet Soil Image**	**Dry Soil Image**
97.5% sand / 2.5% AC	61		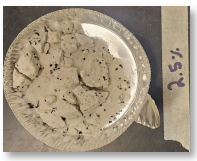
95.0% sand / 5.0% AC	67		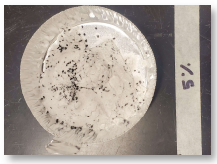
90.0% sand / 10.0% AC	89	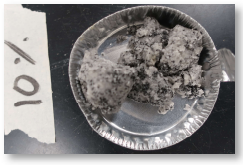	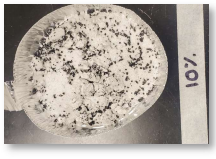

(a)

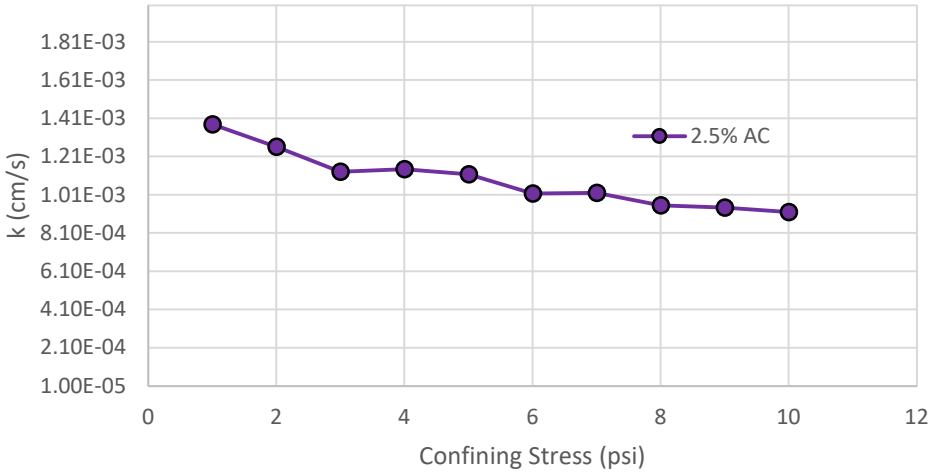

(b)

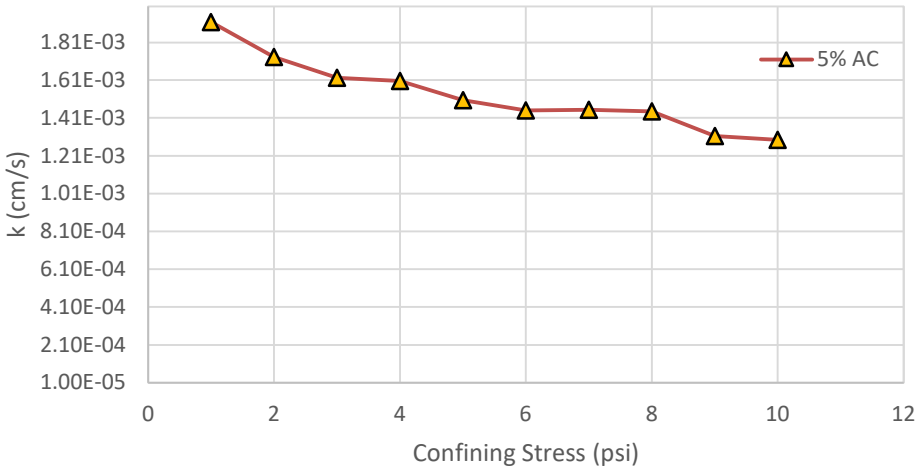

(c)

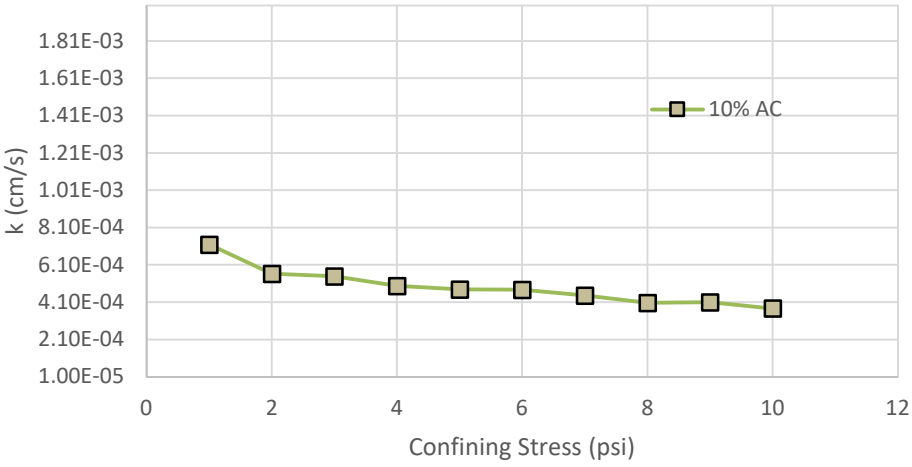

Figure 39: Measured hydraulic conductivity values for sand / AC mixtures: (a) 2.5% AC; (b) 5.0% AC; and (c) 10.0% AC.

4.2 Discussion

4.2.1 F110 Sand

The hydraulic conductivity of F110 sand was used as the base line for comparison of the tests that were performed during this study, and changes in the conductivity and density were compared as a function of porous additive volume. The specific attributes that were of interest focused on hydraulic conductivity and drainage of fly ash in ponded conditions. Take and Beddoe (2014) reported the hydraulic conductivity of F110 sand k = 1×10^{-4} m/s [40], which compared well with the values measured in this study, which averaged $1x10^{-5}\frac{m}{s}$ for sieved F110. The order of magnitude difference with the reference data is attributable to the removal of the larger grain sizes by sieving through a number 70 sieve, retaining the finer F110 sand particles, leaving a finer particle size in the final sand grain size distribution. The hydraulic conductivity tests performed on 100% sieved F110 sand decreased 4.4 $x10^{-3}\frac{cm}{s}$ over a 62.1 kPa (9-psi) increase in confining stress, which is typical behavior for flow in particle media as the pore space decreases in volume due to increased levels of confinement on the specimen.

4.2.2 Implications of the experiment's density preparation

The experiments in this study were performed with a controlled method for preparation. This controlled method involved a mixing process in sealed buckets. The material was placed into the buckets and shaken for minimum of 10 minutes between each test (relative density testing and hydraulic conductivity testing). The volumes of each hydraulic conductivity test were specifically calculated to hold the correct volume of the

material. The volumes of the porous stones, top and end platens locations relative to the mold, and volume of the mold were used to accurately predict the correct volume portions needed for each triaxial set up (a total of 3 cell set ups), and the volume calculations can be seen in Appendix D. After the volume was calculated, each material was dried at $110 \pm 0.5\,°C$. Each of the materials were placed into clean pans and oven dried in between experimental trials. Samples were prepared by pouring the samples into the membrane lined mold through a funnel (Figure 40) that was maintained above the mixture surface of 1.27 cm to 2.54 cm (0.5 inch to 1 inch). A metal tamper was used to compact the material for each layer in 25 medium to moderate drops in a circular pattern of tamping following along the perimeter of the mold for each layer. The compaction effort was held uniform between each of the tests.

Figure 40: Metal tamping rod (left) used and cleaned/dried for each test next to funnel used for 2.5% components (right).

Once each layer was completed and compacted, an additional 4 soft tamps on the inner side of the mold to drop additional fines attached to the tamper followed by an additional 8 tamps made to the out sides of the mold (evenly placed on left and right side of the mold). Then the handle side of the spoon was used to scrape the surface of each layer created in order to avoid layering effects during testing (Figure 41). This process was repeated until the mold was filled or the targeted volumes of soil were filled (approximately 3 to 4 layers).

Figure 41: Image of scraped surface to avoid layering effects.

The relative densities achieved in these experiments were in the zone measured between the minimum and maximum densities; however, the relative densities varied for the specimens that were tested. The target density of the diatomaceous earth mixtures was

achieved in each of the six sample preparations, and was in a range of relative density from 51.0 to 60.0% for the mixtures with sand/diatomaceous earth. The introduction of DE to the sand mixture resulted in a wider grain size distribution, increasing the percentage of finer material. However, this was not true for the activated carbon mixtures. At mixture percentages with low volumes of AC (2.5 to 5.0%), the blend of the material was controlled between 61.0 to 67.0%, but when the mixture percentage was increased to 10.0% AC, the relative density peaked as it reached very close to the maximum density measured in the limiting void ratio tests. The high volume activated carbon mixtures were difficult to control during compaction, and resulted in over compacted specimens that achieved close to maximum relative density. Comparing the 10.0% diatomaceous earth / sand mixture to F110 sand demonstrated that the DE filled the void spaces and decreased the hydraulic conductivity of the material. The final mixture of sand/DE was able to hold its shape very easily in an oven dried state below (Figure 42).

Figure 42: 10.0% DE and F110 during density test

4.2.3 Hydraulic conductivity: Impacts of Diatomaceous Earth

The hydraulic conductivity tests performed in this study were designed to determine the impact of highly porous components in porous media. Comparing hydraulic conductivity of sand/DE mixtures as a function of confining stress demonstrated that increasing the volumes of fines to 10.0% (i.e., DE) mixed with the sand resulted in decrease in hydraulic conductivity when compared to the 100% sand mixtures (Figure 43).

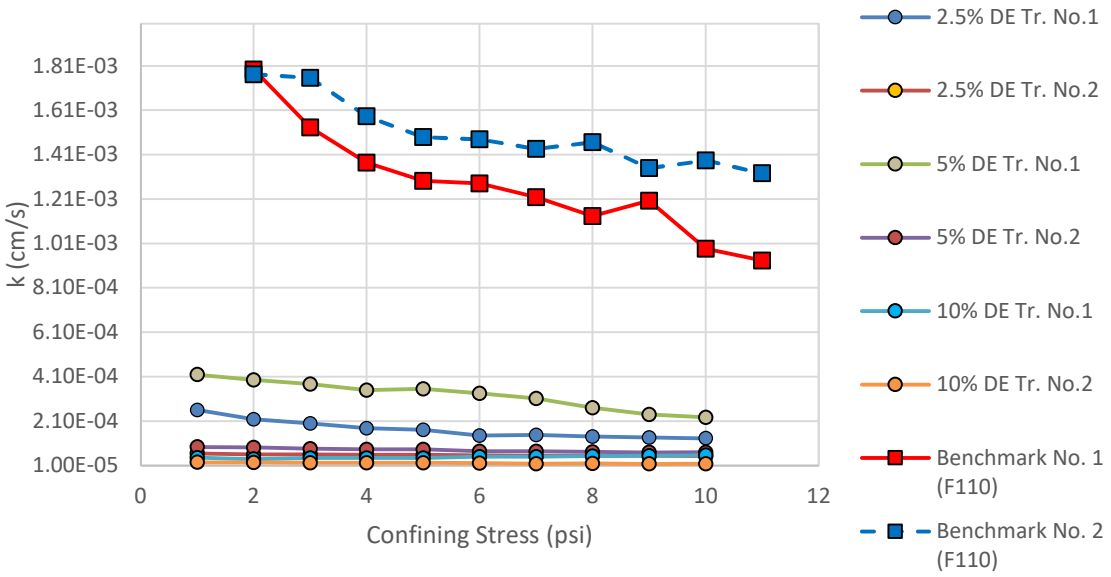

Figure 43 : Hydraulic conductivity as a function of confining stress for 100% sand, compared with 2.5%, 5.0%, and 10.0% sand/DE mixtures.

4.2.4 Hydraulic conductivity: Impacts of Activated Carbon

Similar to the trends that were observed for diatomaceous earth, the mixtures with activated carbon showed decreases in the hydraulic conductivity when compared to the 100% sample, but relatively little variation in magnitude between the tested mixtures (

Figure 44). Measured hydraulic conductivity values for the mixtures demonstrated less than one order of magnitude in variation, with no clear trend in the 2.5 and 5.0% AC mixtures.

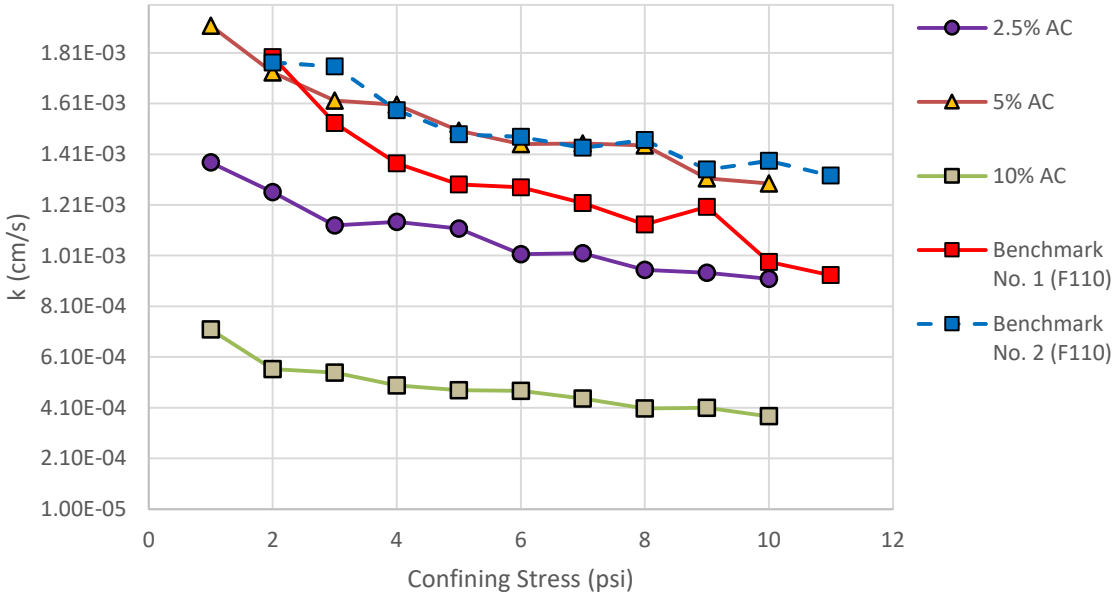

Figure 44: Hydraulic conductivity as a function of confining stress for 100% sand, compared with 2.5%, 5.0%, and 10.0% sand/AC mixtures.

Figure 43 and Figure 44 show the sensitivity difference in k $\left(\frac{cm}{s}\right)$ of blended materials (DE and AC) to a pure F110 sand with increasing confining stress. This happens because F110 sand contains unfilled pore space that is more compressible, while the blends on the other hand have pore spaces filled by the porous components making them less compressible.

CHAPTER 5 CONCLUSION AND RECOMMENDATIONS FOR FUTURE WORK

5.1 Conclusion

During this study, fly ash was studied in a series of characterization and engineering tests to investigate and quantify hydraulic conductivity, with emphasis on fly ash hydraulic conductivity and water retention observed in fly ash ponds. The work performed distinguished the regimes in terms of the balance of forces between gravitational and capillary forces that are the two potential driving forces during drainage of fly ash deposits. The primary variable that determines when these soils reach drainage equilibrium is linked to the mean pore size.

Experiments were performed that used the details developed in the theoretical analysis to carefully select porous components that were found in fly ash (diatoms and unburned carbon), and were tested in the forms of fresh water diatomaceous earth and commercially produced activated carbon. This study controlled the volumes of these two components by introducing them to a high permeability and controllable material (Fine F110 sand) to effectively detect the subtle changes in the hydraulic conductivity, even at low percentages (2.5%, 5.0%, and 10.0%). The porous components were characterized using SEM, specific gravity tests, and measurement of limiting void ratios and densities. This information was used to develop bulk samples of the mixtures in a controlled method using F110 sand as a base and a benchmark for the porous components. Six bulk samples were prepared (2.5% DE and AC, 5.0% DE and AC, and 10.0% DE and AC) for testing. The work performed in this study then investigated the hydraulic properties of the

simulated particulate mixtures. The following conclusions can be drawn from these experiments:

- As the data indicated, the % of high porosity components in the mixture had significant impact on the fabric and structure of the mixtures. For mixtures with high porosity additives, e_{max} increased in all cases (from 0.84 with 100% sand to 1.37 for the sample with 10.0% DE / 90.0% sand and from 0.84 with 100% sand to 0.98 for the sample with 10.0% AC / 90.0% sand).
- The minimum void ratio for mixtures with high porosity components increased as additional percentage volumes of DE were added at lower percentages, but plateaued after the initial increase of porosity (initial increase from 0.55 with 100% sand to 0.59 averaged across all of the samples at 2.5%, 5.0%, and 10.0% DE samples).
- These tests also indicate that AC showed a significantly larger rate of increase in porosity when compared to the DE mixtures, as it exhibited an overall larger increase in both e_{max} and e_{min}. For example, e_{min} increased in each additional sample with increasing percentage volumes of AC (from 0.55 with 100% sand to 0.58 with 2.5% AC / 97.5% F110 to 0.62 with 5.0% AC / 95.0% F110 and lastly 0.68 for with 10% AC / 90.0% F110).
- Results that link diatomaceous earth to a significant reduction in hydraulic conductivity at lowest percentages are comparable to those of a silt material indicating the DE particles were small enough to fill the void spaces of the sand matrix, while the AC particles had a larger range in grain sizes, and both packed void space and displaced sand grains. Addition of these highly porous

components acted to reduce the hydraulic conductivity, and will also act to retain water in partially saturated conditions due to high capillary forces within their highly porous structure.

- Measured values of hydraulic conductivity indicated that the highly porous diatom components decreased the saturated hydraulic conductivity by one to two orders of magnitude. For activated carbon mixtures, hydraulic conductivity decreased one order of magnitude.

5.2 Recommendations for future work

After the experiments and analysis were conducted, it was clear that the addition of high porosity components at low percentages in the particulate media displays a direct correlation to reduced drainage performance. Future studies and testing can certainly take this further by in introducing the presence of combined volume percentages of highly porous components (DE and AC split evenly to achieve 2.5%, 5.0%, and 10.0% with highly porous components) and also testing purely porous components for its relative density and hydraulic conductivity. These tests will operate with controlled relative densities that correlate the effects of hydraulic conductivity to confining stress, volume percent additives, and averaged specific surface areas of blends. These tests primarily point to the drainage performance as a good indication that high water retention capacity exists in the fly ash due to the presence of the components, and can build upon this premise by implementing new and innovative tests that further test their capacity and effects on the fly ash by:

- Simulating ash pond conditions (fully and partially submerged fly ash over prolonged periods of time (1 month, 2months, 3 months etc.)) that will be used for:
    - Hydraulic Conductivity Testing
    - Study of presence of capillary condensation via SEM analysis
    - Wetting / drying experiments using p-wave velocity to identify fully saturated conditions

*(Where all tests are conducted before and after ash pond simulated conditions)

- Studying live diatom replication and growth via SEM with fly ash from simulated pond conditions that isolate the effects of:
    - Nutrients like Nitrate, Sulfur, and Silicon Dioxide
    - Sunlight (exposure vs no exposure)

- Testing porous component retention capacities with soil water characteristic curves (SWCC) on:
    - DE
    - AC
    - F110
    - Fly ash

APPENDIX A. DIATOMITE PROPERTY VALUE REFERENCE [41]

Table 3. **Property Ranges of Diatomite Products**[a,b]

Property	Filter aids			Fillers, all types
	Natural	Calcined	Flux-calcined	
permeability range, μm^2[c]	0.06	0.5–2.0	1.0–29.6	
density, kg/m^3				
wet cake	240–350	270–350	290–380	
bulk	112	120–128	144–336	104–160
particle size distribution (granulometer), μm				
10% less than	1.5–3.6	2.5–4.4	7–11	2–4
50% less than	7.0–13.4	10.0–16.1	25–37	6–20
90% less than	25–44.5	30.0–58.9	65–97	14–30
approximate pressure differential[d], kPa[e]	36.5	2.33–4.56	1.11–0.058	
specific gravity	2.00	2.25	2.33	2.0–2.3
porosity, by volume, %	65–85	65–85	65–85	65–85
median pore size range, μm	1.5	3.5–5.0	7–22	[f]
surface area, m^2/g	10–20	4–6	1–4	0.7–30
pH	6.0–8.0	6.0–8.0	8.0–10.0	6.0–10.0
refractive index	1.42	1.44	1.48	1.40–1.49
oil absorption, %				100–210
particle size, retained %				
98 μm (150 mesh)	1–2	4–7	6–40	
44 μm (325 mesh)	0–12			0–14
Moh's hardness	3.5–4.0	4.5	5.5–6.0	3.5–6.0

[a]Values given are typical or estimated values, not specifications.
[b]Refs. 10–12.
[c]To convert from μm^2 to d'Arcys, multiply by 1.013.
[d]Measurement at 0.034 cm/s and 0.1 g/m^2 precoat.
[e]To convert from kPa to psi, multiply by 0.145.
[f]The Hegman gauge readings, useful for paint manufacture, run from 0–55.

APPENDIX B. SPHERICAL SILICA BEADS QUALITY CONTROL

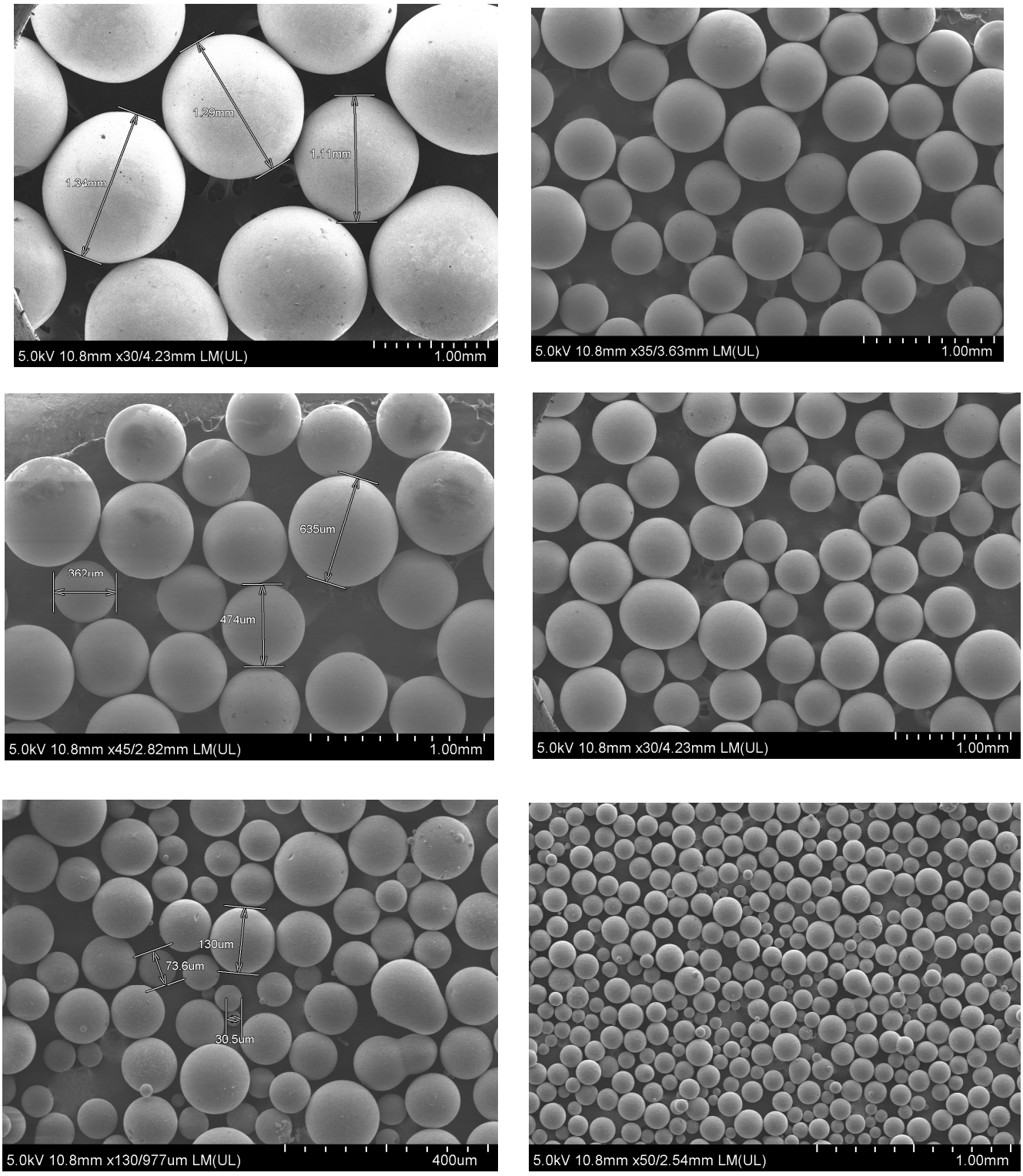

Figure 1B: SEM Images of (Top to Bottom (1mm, .5mm, and .01 mm) bead

APPENDIX C. VOLUME BLEND SAMPLE CALCULATIONS

Sample Calculation for 2.5%DE/97.5%F110 on hydraulic conductivity test:

Table 1C: List of assumptions

Gs Sand	2.67
Gs DE	2.23
Assumed Vtotal (cm^3)	64.56
% Sand	97.5%
% DE	2.5%
Dr (target)	95.0%
e (assumed)	0.6
ρwater (g/cm^3)	1
Vvoids	24.21
Vsolids	40.35

Develop system of equations based on phase diagram containing air, sand, and diatomaceous earth. This will use the specific gravity from tests and will assume void ratio is 0.6. The primary unknowns are VDE, Vsand, MDE, and Msand.

Table 2C: System of equations

Vtotal = Vair+Vwater+Vsand+VDE	64.56	cm^3				
Vvoid = Vair + Vwater = e*Vs = 0.6 Vsand + 0.6 VDE						
Vtotal = 0.6 Vsand + 0.6 VDE +						
Vsand+VDE=	64.56	cm^3				
Vtotal =	64.56	cm^3 =	1.6	Vsand +	1.6	VDE
ρDE = (Msand/Vsand)						
Msand = Vsand*ρsand =Gs Sand*ρwater*Vsand						
Msand = Gs Sand*ρwater*Vsand = 2.67*1(g/cm^3)*Vsand =				2.67	Vsand	
ρDE = (MDE/VDE)						
MDE = VDE*ρDE =Gs DE*ρwater*VDE						
MDE = Gs DE*ρwater*VDE = 2.23*1(g/cm^3)*VDE =				2.23	VDE	
MDE = Mtot*		2.50%				
Msand = Mtot*		97.50%				
MDE = .025*(Msand/.975) =		0.025641	Msand			
39	MDE = Msand					

Table 3C: Plug into solver and find the unknown variables

Unknowns: Vsand,VDE,MDE,Msand Plug these four equations and unknowns into solver and scale to appropriate size for test	
Vsand	39.1481
VDE	1.20186
MDE	2.68014
Msand	104.526

Phase diagrams in excel will calculate the same values based on two of the volumes to double check your values are correct. The volume is based on volume size of mold for vibratory test or hydraulic conductivity tests (Figure 4C):

Panel No.1	
Volume of Sample (cm^3)	64.56

Volume (cm^3)		Volume of mold	Mass (g)	
Vair/Vvoids=	24.21004	air	Mair =	0
Vwater=	0	water	Mwater=	0
Vsand=	39.1481	Sand	Msand=	104.5254
VDE=	1.20186	DE	MDE=	2.680148

Figure 4C: Phase diagram automated calculations.

APPENDIX D. VOLUME SAMPLE CONTROL CALCULATION EXCEL TEMPLATE

Table 1D: Porous stone and end platen measurements

Panel No.1 DE Tr. No. 1		
	Height (cm)	Diameter (cm)
Base Platen	3.18	3.56
Top platen	2.54	3.54
Bottom stone (white edging)	0.64	3.52
Top stone	0.63	3.51

Table 2D: Mold measurements

	Height (mm)	Diameter (mm)	Height (cm)	Diameter (cm)
Mold Base	32.36	41.45	3.24	4.15
Mold Shaft	76.01	35.80	7.60	3.58

Table 3D: Volume of sample calculations

Volume Top Stone (cm^3)	6.22
Height or portion of porous stone below the of the mold base	0.05
Volume of Bottom Stone above the top of the mold base (cm^3)	5.72
Volume of Mold Shaft (cm^3)	76.50
Volume of Sample (cm^3)	64.56

APPENDIX E. DERIVATION OF CAPILLARY PRESSURE AND ITS LINK TO MEAN PORE SIZE

Explanation of capillary pressure

$$\mu - \mu_{sat}(T) = \frac{P_l - P_{sat}(T)}{P_l} = kT \ln\left(\frac{P_v}{P_{sat}(T)}\right) = kT \ln(RH) \rightarrow P_l = P_{sat}(T) + KT\rho_l \ln(RH) \quad \textbf{(1)}$$

$$P_l - P_v = P_c = (1 - RH)P_{sat}(T) + KT\rho_l \ln(RH) \quad \textbf{(2)}$$

Use of Gibbs-Duhem equation as a governing law in the model.

$$VdP - Nd\mu - SdT = 0 \rightarrow |dP|_T = \rho d\mu \; with \; \rho = \frac{N}{V} \quad \textbf{(3)}$$

Assume that the vapors acting within the pore space of the clays are ideal gases.

$$\rho = \frac{P}{kT} \rightarrow dln(P_v) = \frac{1}{kT} d\mu \rightarrow \ln\left(\frac{P_v}{P_{sat}(T)}\right) = \frac{1}{kT}(\mu - \mu_{sat}(T)) \quad \textbf{(4)}$$

Assuming that the liquid acting within the fly ash is nearly incompressible will allow the development of the following relationship.

$$\rho_l = Cte \quad \textbf{(5)}$$

$$dP_l = \rho_l d\mu \rightarrow P_l - P_{sat}(T) = \rho_l(\mu - \mu_{sat}(T)) \quad \textbf{(6)}$$

Finally, all of the following assumptions can be used to link pore size with Laplace law.

$$P_l - P_v = \frac{2\gamma}{r} \quad \textbf{(7)}$$

$$r \approx \frac{2\gamma}{kT\rho_l \ln(RH)} \quad \textbf{(8)}$$

APPENDIX F. XENIA WIRTH DIATOM SEMS FOUND IN FLY ASH

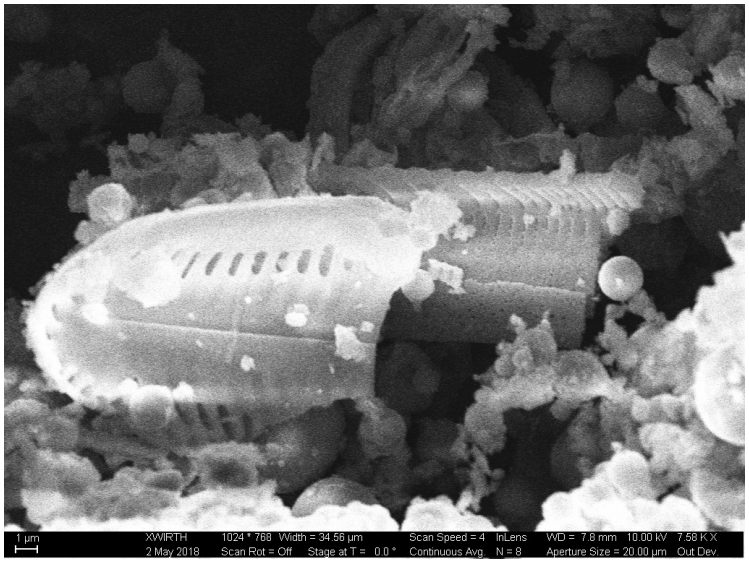

Figure 1F: SEM of diatom found in fly ash sample

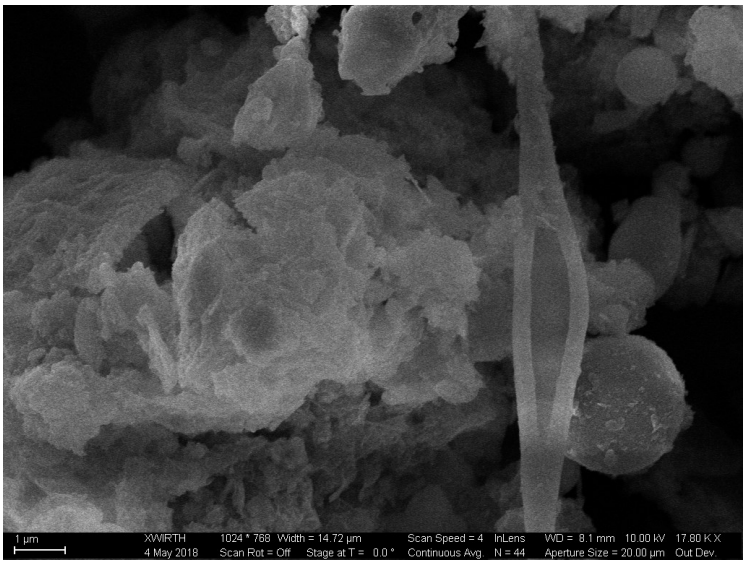

Figure 2F: SEM of diatom found in fly ash sample

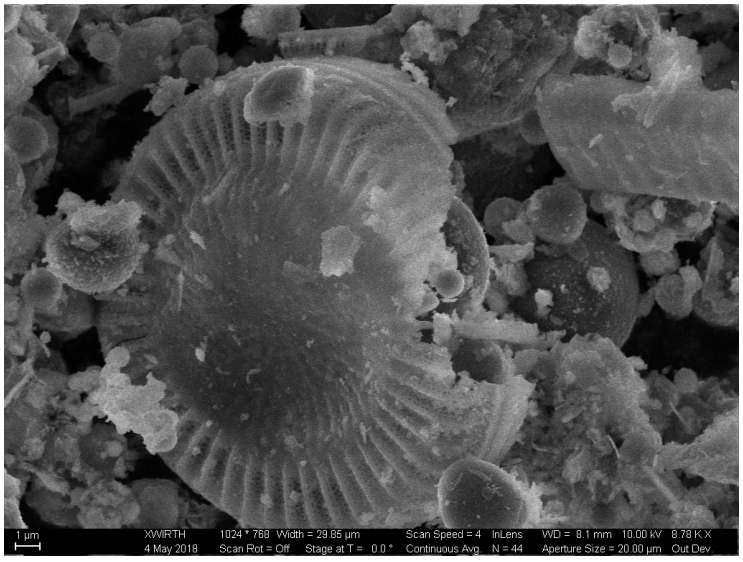

Figure 3F: SEM of diatom found in fly ash sample

Figure 4F: SEM of diatom found in fly ash sample

APPENDIX G. DIATOM GEOMETRICAL ANALYSIS

[42]

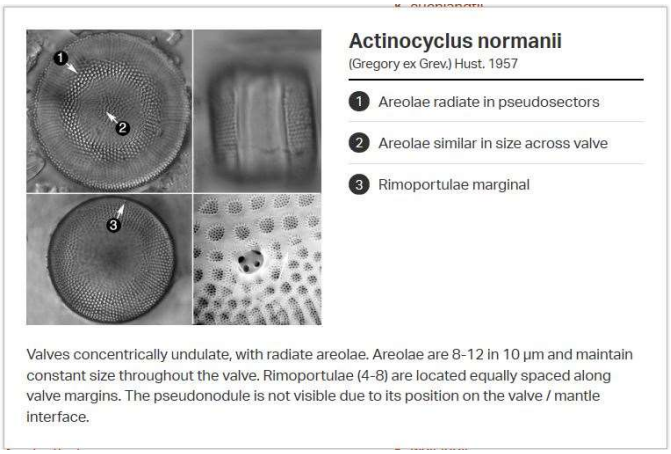

Figure 1G: Actinocyclus normanii

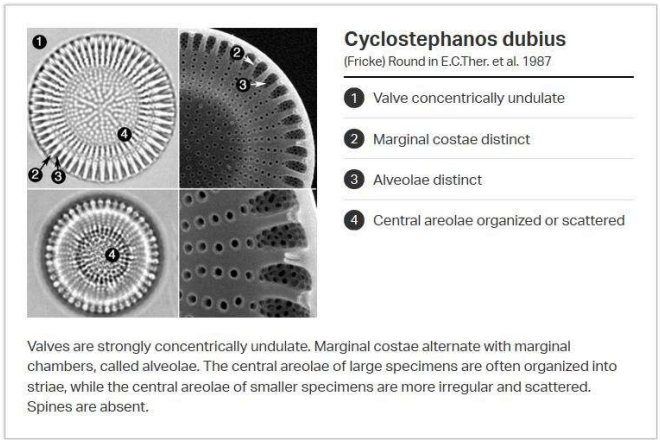

Figure 2G: Cyclostephanos dubius

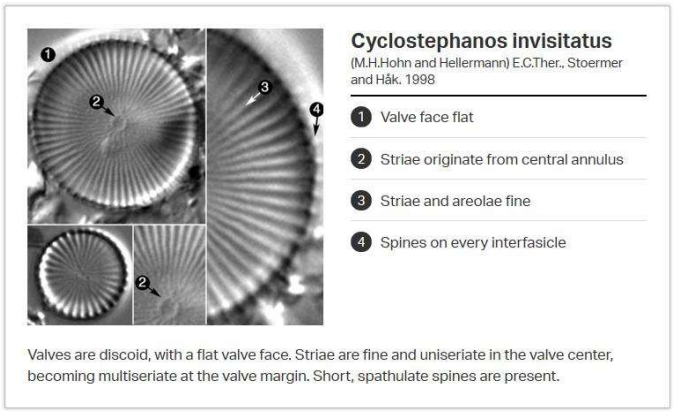

Figure 3G: Cyclostephanos Invistatus

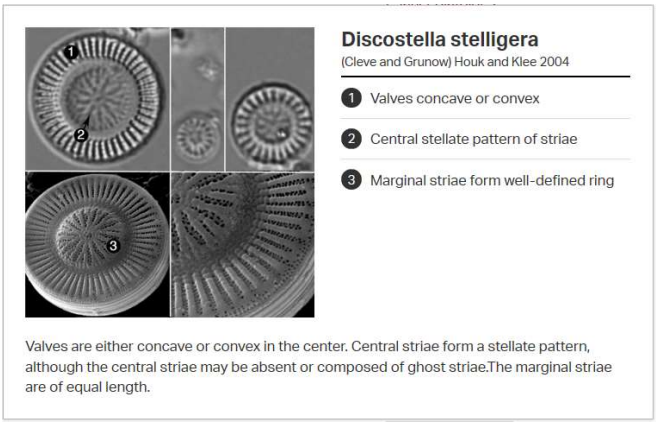

Figure 4G: Discostella Stelligera

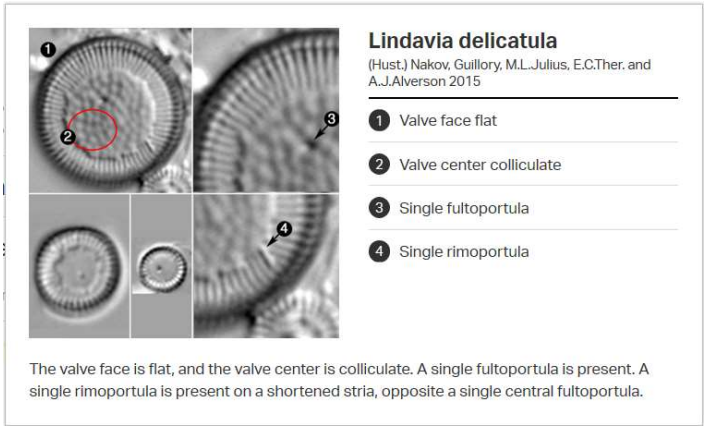

Figure 5G: Lindavia delicatula

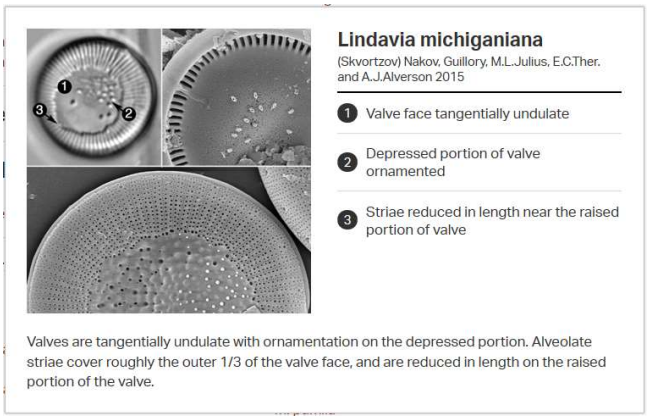

Figure 6G: Lindavia michiganiana

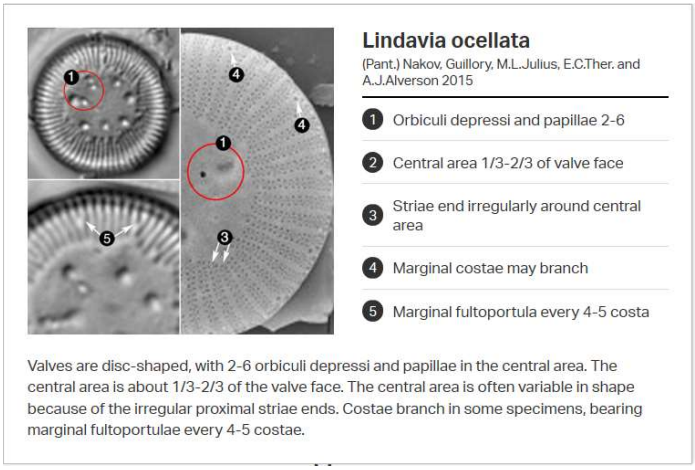

Figure 7G: Lindavia ocellata

REFERENCES

[1]. "U.S. Energy Information Administration - EIA - Independent Statistics and Analysis." *U.S. Energy Facts Explained - Consumption and Production - U.S. Energy Information Administration (EIA)*, www.eia.gov/energyexplained/us-energy-facts/.

[2]. Ritchie, Hannah, and Max Roser. "Fossil Fuels." *Our World in Data*, 2 Oct. 2017, ourworldindata.org/fossil-fuels.

[3]. Rosenberg, Ronald H. "Making renewable energy a reality-Finding ways to site wind power facilities." Wm. & Mary Envtl. L. & Pol'y Rev. 32 (2007): 635.

[4]. "U.S. Energy Information Administration - EIA - Independent Statistics and Analysis." *Use of Coal - U.S. Energy Information Administration (EIA)*, 2020, www.eia.gov/energyexplained/coal/use-of-coal.php.

[5]. Shwartz, Mark. "Q&A: Stanford Expert Explains Why We Continue Burning Coal for Energy." *Energy*, Q&A: Stanford Expert Explains Why We Continue Burning Coal for Energy, 20 Dec. 2019, energy.stanford.edu/news/qa-stanford-expert-explains-why-we-continue-burning-coal-energy.

[6]. Möllersten, K., Yan, J., & R. Moreira, J. (2003). Potential market niches for biomass energy with CO2 capture and storage—Opportunities for energy supply with negative CO2 emissions. Biomass and Bioenergy, 25(3), 273–285. https://doi.org/10.1016/s0961-9534(03)00013-8

[7]. American Coal Ash Association. (2003, June 13). Chapter 1 - Fly Ash - An Engineering Material - Fly Ash Facts for Highway Engineers - Recycling - Sustainability - Pavements - Federal Highway Administration. Https://Www.Fhwa.Dot.Gov/Pavement/Recycling/Fach01.Cfm.

[8]. Ramme, Bruce W., and Mathew P. Tharaniyil . "Coal Combustion Products Utilization Handbook." Https://Www.acaa-Usa.org/, We Energies, 2013, www.acaa-usa.org/Portals/9/Files/PDFs/ccp_utilization_handbook.pdf.

[9]. "Pavements." Fly Ash Facts for Highway Engineers, U.S. Department of Transportation Federal Highway Administration, 27 June 2017, www.fhwa.dot.gov/pavement/recycling/fach01.cfm.

[10]. Pugh, John, et al. "Five+ Year Evaluation of an Engineered Fill with Recycled Coal Combustion Products." TRID, 30 Nov. 2014, trid.trb.org/view/1336852.

[11]. "Coal Ash Spill, Tennessee." *NASA*, NASA, earthobservatory.nasa.gov/images/36352/coal-ash-spill-tennessee.

[12]. Erwin, Nicole. "Tennessee Meteorite Site at Center of TVA Coal Compliance Issue." WKMS , WKMS, Murray State's NPR Station, 13 Dec. 2016, www.wkms.org/post/tennessee-meteorite-site-center-tva-coal-compliance-issue.

[13]. Dewan, Shaila. "Coal Ash Spill Revives Issue of Its Hazards." The New York Times, The New York Times, 25 Dec. 2008, www.nytimes.com/2008/12/25/us/25sludge.html?auth=login-facebook.

[14]. Patterson, Brittany. “The Cautionary Tale of the Largest Coal Ash Waste Site in the U.S.” The Allegheny Front, The Allegheny Front, 29 July 2020, www.alleghenyfront.org/the-cautionary-tale-of-the-largest-coal-ash-waste-site-in-the-u-s/.

[15]. U.S. Department of Transportation/. User Guidelines for Waste and Byproduct Materials in Pavement Construction, U.S. Department of Transportation/Federal Highway Administration, 2016, www.fhwa.dot.gov/publications/research/infrastructure/structures/97148/cfa53.cfm.

[16]. Carrier, W. David. “Goodbye, Hazen; Hello, Kozeny-Carman.” *Journal of Geotechnical and Geoenvironmental Engineering*, American Society of Civil Engineers, 15 Oct. 2003, ascelibrary.org/doi/10.1061/%28ASCE%291090-0241%282003%29129%3A11%281054%29.

[17]. Amr F. Elhakim, Estimation of soil permeability, Alexandria Engineering Journal, Volume 55, Issue 3, 2016, Pages 2631-2638, ISSN 1110-0168, https://doi.org/10.1016/j.aej.2016.07.034.

[18]. Vesperman, KD, et al. “STP874.” *ASTM International - Standards Worldwide*, ASTM International, 1985, www.astm.org/DIGITAL_LIBRARY/STP/PAGES/STP34586S.htm.

[19]. Bartholomew, Calvin H., et al. “Accurate Determination of Pore Size Distributions Of Catalysts and Supports: Emphasis on Alumina.” Departments of Chemical Engineering and Chemistry, Brigham Young University.

[20]. Schmitz, Karl Uwe. “Flocculation and Coagulation - Floc Forming and Particle Settling.” *YouTube*, Karl-Uwe Schmitz, 20 July 2019, youtu.be/JkpMWjW3wbE.

[21]. Pegues , James C. “2.0.” *CCR Surface Impoundment Emergency Action Plan*, 2nd ed., Plant Hammond Ash Pond, Georgia Power, 2018, pp. 2–2. AP-2.

[22]. Wirth, Xenia. “BENEFICIAL USE OF BIOMASS AND COAL COMBUSTION RESIDUALS .” *Georgia Institute of Technology*, Georgia Institute of Technology, 2019, pp. 1–180.

[23]. Yeboah, N.N. Nortey, et al. “Characterization of Biomass and High Carbon Content Coal Ash for Productive Reuse Applications.” *Fuel*, Elsevier, 27 Aug. 2013, www.sciencedirect.com/science/article/pii/S0016236113007588.

[24]. Kim, Bumjoo, et al. “Geotechnical Properties of Fly and Bottom Ash Mixtures for Use in Highway Embankments.” Journal of Geotechnical and Geoenvironmental Engineering, vol. 131, no. 7, 2005, pp. 914–924., doi:10.1061/(asce)1090-0241(2005)131:7(914).

[25]. Mollamahmutoğlu, M., Yilmaz, Y. Potential use of fly ash and bentonite mixture as liner or cover at waste disposal areas. Env Geol 40, 1316–1324 (2001). https://doi.org/10.1007/s002540100355

[26]. Prashanth, J. & Puvvadi, Sivapullaiah & Sridharan, A.. (2001). Pozzolanic fly ash as a hydraulic barrier in land fills. Engineering Geology - ENG GEOL. 60. 245-252. 10.1016/S0013-7952(00)00105-8.

[27]. De Stefano, Mario, and Luca De Stefano. "Nanostructures in Diatom Frustules: Functional Morphology of Valvocopulae in Cocconeidacean Monoraphid Taxa." *Journal of Nanoscience and Nanotechnology*, U.S. National Library of Medicine, 2005, pubmed.ncbi.nlm.nih.gov/15762156/.

[28]. "Identifying Marine Diatoms and Dinoflagellates." Edited by Carmelo R. Tomas, *ScienceDirect*, Elsevier, 1996, www.sciencedirect.com/book/9780126930153/identifying-marine-diatoms-and-dinoflagellates.

[29]. Lindsey, Rebecca, and Robert Simmon. "What Are Phytoplankton?" *NASA*, NASA, 2010, earthobservatory.nasa.gov/features/Phytoplankton.

[30]. US Department of Commerce, National Oceanic and Atmospheric Administration. "What Are Phytoplankton?" *NOAA's National Ocean Service*, NOAA, 27 July 2009, oceanservice.noaa.gov/facts/phyto.html.

[31]. ZHANG , DeYuan, et al. "Bio-Manufacturing Technology Based on Diatom Micro- and ..." *Springer Link*, Chinese Science Bulletin, 2012, link.springer.com/content/pdf/10.1007%2Fs11434-012-5410-x.pdf.

[32]. Hamm, C., Merkel, R., Springer, O. *et al.* Architecture and material properties of diatom shells provide effective mechanical protection. *Nature* 421, 841–843 (2003). https://doi.org/10.1038/nature01416

[33]. Wirth, Xenia, et al. "(PDF) Evaluation of Alternative Fly Ashes as Supplementary ..." *Researchgate*, 2019, www.researchgate.net/publication/333707620_Evaluation_of_Alternative_Fly_Ashes_as_Supplementary_Cementitious_Materials.

[34]. Diatoms: Definition, Characteristics & Types. (2015, August 25). Retrieved from https://study.com/academy/lesson/diatoms-definition-characteristics-types.html.

[35]. "Diatomaceous Earth." *Encyclopædia Britannica*, Encyclopædia Britannica, Inc., www.britannica.com/science/diatomaceous-earth.

[36]. Marsh, Harry, and Reinoso Francisco Rodríguez. *Activated Carbon*. Elsevier, 2006.

[37]. Callewaert, Jeroen. "Carbonology." *Desotec*, DESOTEC Activated Carbon Research and Development , 2014, www.desotec.com/en/carbonology/carbonology-cases/activated-carbon-pores.

[38]. Wirth, Xenia & Burns, S. & Glatstein, Daniel. (2018). Mineral Phases and Carbon Content in Weathered Fly Ashes. Fuel. 236. 10.1016/j.fuel.2018.09.106.

[39]. "Activated Carbon Production." *YouTube*, Зелинский Групп, 15 May 2019, youtu.be/KZ4nIHJqm0o.

[40]. Take, W. & Beddoe, Ryley & Davoodi, Roya & Phillips, Ryan. (2014). Effect of antecedent groundwater conditions on the triggering of static liquefaction landslides. Landslides. 12. 10.1007/s10346-014-0496-7.

[41]. Othmer, Kirk. “Kirk-Othmer Encyclopedia of Chemical Technology.” *Wiley Online Library*, 1947, onlinelibrary.wiley.com/doi/book/10.1002/0471238961.

[42]. Diatoms of North America. “Species.” Diatoms.org, Diatoms of North America, 2020, diatoms.org/species.

[43]. ASTM Standards

a. ASTM D 4253: Standard Test Methods for Maximum Index Density and Unit Weight of Soils Using a Vibratory Table

b. ASTM D 4254: Standard Test Methods for Minimum Index Density and Unit Weight of Soils and Calculation of Relative Density

c. ASTM D5084-16A: Standard Test Methods for Measurement of Hydraulic Conductivity of Saturated Porous Materials Using a Flexible Wall Permeameter

d. ASTM D 854: Standard Test Methods for Specific Gravity of Soil Solids by Water Pycnometer

e. ASTM D6913: Standard Test Methods for Particle-Size Distribution of Soils Using Sieve Analysis